

Transition Metal-Vacancy Point Defects in Zinc Oxide as Deep-Level Spin Qubits

Shimin Zhang,¹ Taejoon Park,^{2,3,*} Erik Perez,^{1,*} Kejun Li,¹ Xingyi Wang,⁴ Yanyong Wang,⁵ Jorge D Vega Bazantes,⁵ Ruiqi Zhang,⁵ Jianwei Sun,⁵ Kai-Mei C. Fu,^{6,4,7} Hosung Seo,^{2,8,3,9,†} and Yuan Ping^{1,10,11,‡}

¹*Department of Materials Science and Engineering, University of Wisconsin-Madison, 53706, USA*

²*SKKU Advanced Institute of Nanotechnology, Sungkyunkwan University, Suwon, Gyeonggi 16419, Korea*

³*Department of Energy Systems Research and Department of Physics, Ajou University, Suwon, Gyeonggi 16499, Korea*

⁴*Department of Electrical and Computer Engineering, University of Washington, Seattle, WA, 98195, USA*

⁵*School of Science & Engineering, Tulane University, 6823 St Charles Ave, New Orleans, LA 70118, USA*

⁶*Department of Physics, University of Washington, Seattle, WA, 98195, USA*

⁷*Physical Sciences Division, Pacific Northwest National Laboratory, Richland, Washington 99352, USA*

⁸*Department of Quantum Information Engineering, Sungkyunkwan University, Suwon, Gyeonggi 16419, Korea*

⁹*Center for Quantum Information, Korea Institute of Science and Technology, Seoul 02792, Korea*

¹⁰*Department of Physics, University of Wisconsin-Madison, 53706, USA*

¹¹*Department of Chemistry, University of Wisconsin-Madison, 53706, USA*

(Dated: February 4, 2025)

Zinc oxide (ZnO) is a promising candidate for hosting point defects as spin qubits for quantum information applications, due to its wide band gap, low spin-orbit coupling, and dilute nuclear spin environment. Previously shallow impurities in ZnO were mostly proposed for spin qubit candidates, but deep-level spin defect studies in ZnO are rather sparse, which may be ideally decoupled from the host materials for stable operation. In this work, we theoretically search for deep-level point defects in ZnO with optimal physical properties suitable for optically-addressable spin qubits in the solid-state. Using first-principles calculations for the search, we have predicted the Mo vacancy defect in ZnO owning promising spin and optical properties, including spin-triplet ground state, optical transition in the visible to near-infrared range with high quantum yield, allowed intersystem crossings with a large optically-detected magnetic resonance contrast, and long spin T_2 and T_2^* . Notably, we found the Huang-Rhys factor of the defect to be around 5, which is much smaller than those at 10-30 of the most-known defects in ZnO. We also proposed a new protocol for initializing and reading spin qubits, which could be applied in other systems with forbidden longitudinal intersystem crossing. Finally, we compared the spin decoherence driven by the nuclear spin bath and by paramagnetic impurity baths. We found that the paramagnetic impurities are very effective in causing spin decoherence even with very low concentrations, implying that the spin decoherence in ZnO can be likely dominated by them even after isotopic purification.

I. INTRODUCTION

Point defects in wide band gap solids, particularly with unpaired spins, are emerging as promising candidates for quantum bits (qubits) in spin-based quantum information science due to their superior advantages such as room-temperature operation and long coherence times. Accordingly, the discovery of new spin qubit candidates is a fast-growing field of research to find the best-ever systems that can advance existing quantum technologies or enable entirely new capabilities. Such efforts led to the discovery of group-IV-vacancy qubits in diamond [1–4], vacancy spins in SiC [5, 6], and more recently, boron vacancy spins in hexagonal boron nitride [7–9]. Notably, first-principles theoretical approaches played an essential role in identifying these candidates by efficiently explor-

ing the vast configuration space of defects in a material, narrowing down to the best candidates, and navigating the unknown between desirable qubit properties and the defect structure.

The search for impeccable quantum defects for spin qubits requires consideration of both defect and host material. An ideal host material for spin qubits requires several key properties: a wide band gap in which ground and excited defect levels lie within the gap, a nuclear spin density as low as possible to enhance coherence times, and the availability of high-quality single crystals to minimize unwanted defects and impurities [10]. Given a host material, a sequence of criteria can be considered to identify the best qubit candidate, such as deep defect levels, high-spin states, high radiative recombination rates over non-radiative processes, weak electron-phonon coupling or large Debye-Waller factor, and long spin relaxation and coherence times [11–13].

In such considerations, ZnO recently stood out as a promising candidate as a superb host material. It can be grown with extremely high purity using molecular beam

* SZ, TP, and EP contributed equally.

† seo.hosung@skku.edu

‡ yping@wisc.edu

epitaxy (MBE), achieving sub-parts per billion (ppb) residual background impurity concentrations [14, 15]. This high level of purity significantly reduces unintentional defects and magnetic-field noise induced by paramagnetic defects, which are critical for maintaining long coherence times of spin qubits. Furthermore, ZnO benefits from the inherent properties of oxides, where oxygen is 99.7% nuclear-spin-free [16], ensuring a magnetically quiet environment that can further reduce noise and enhance the coherence of spin qubits. Finally, the piezoelectricity properties of ZnO introduce the possibility of strain tuning of quantum states of the spin defects.

In addition, several shallow donors have already been realized as promising candidates for qubits in ZnO with advantageous optical and spin properties. The neutral Indium (In) and Gallium (Ga) donor-bound electron (D^0) are spin-1/2 qubit systems, and they have been reported with long spin relaxation times (T_1) ($>100\text{ms}$) [17, 18], Hahn-spin-echo decoherence times ($T_2 \approx 50\mu\text{s}$) [18], and narrow inhomogeneous linewidth [19, 20]. Experimentally, all-optical methods have been utilized to control the electron spin state of donor qubits at cryogenic temperatures [21].

We remark, however, that it is necessary to expand the scope of spin qubits in ZnO beyond the shallow donors to further advance the current ZnO-based spin-photon interface and to explore new capabilities. It is worth noting that the donor qubits are inherently sensitive to magnetic noise, such as inhomogeneous nuclear fields due to their nanometer-large Bohr radius of the electron wave function [22], making low temperatures essential for their operation [19, 21]. Furthermore, the optical emission of the donor qubits is in the UV range, which is not favorable for long-distance communications by optical fibers. In this regard, it is imperative to search for deep-level defect-based qubit candidates in ZnO that enable room temperature optical initialization, and quantum emission near IR and visible range that can coherently couple to the spin. Unlike the spin 1/2 system of the shallow donors, deep-level defects with a highly localized spin-triplet ground state would show better robustness against the environmental noise and be better suited for quantum sensing applications. Interestingly, several previous studies reported strong quantum emission from deep-level defects in ZnO, but there are no confirmed defects as spin qubits in ZnO so far.

In this article, we investigate a family of substitutional impurity-oxygen vacancy defect complexes and identify Mo vacancy being the most promising spin qubit candidate in ZnO, with superior optical and spin properties for optically-addressable spin-qubits. We found it has remarkable low Huang-Rhys factor (~ 5), compared to other known defects in ZnO (over 10). Consequently we obtain sharp zero-phonon line in photoluminescence lineshape and high quantum yield due to suppressed electron-phonon coupling and phonon-assisted nonradiative processes. Furthermore, we found that the spin coherence T_2 time can be strongly dominated by paramag-

netic impurities, different from the conventional nuclear-spin-limited T_2 . Finally, we found exceptional large non-axial spin-orbit coupling which resulted in strongly polarized inter-system crossing and proposed a new spin initialization and readout protocol for spin qubits with similar spin properties.

II. RESULTS

Inspired by the previously proposed large metal ion-vacancy (LMI vacancy) pairs in 4H-SiC and ω -AlN as promising qubit candidates [23], we construct a similar NV^- -like C_{3v} structure of vacancy complexes in ZnO, consisting of an oxygen vacancy site and a zinc substitution site, as shown in Figure 1, where 'X' is the substitution atom. To identify defects suitable for spin qubits, we follow the workflow outlined in Figure 1. The process begins with a general search for defects with spin triplet ($S=1$) ground states and defect-related optical transition energies within the band gap. We then assess the thermodynamic stability of the defect candidates through defect formation energy and charge transition level calculations. Next we evaluate the zero-phonon line (ZPL), optical dipoles, and radiative lifetime for the suitable emission energy range and optical accessibility. Afterward, we investigate electron-phonon coupling related properties including the Huang-Rhys (HR) factor, non-radiative lifetime, and quantum yield for optimal photon emission efficiency. These steps establish the feasibility of optically-addressable spin qubits.

Next, we examine spin-related properties required for quantum applications. Specifically, the nuclei spin hyperfine interaction influences the spin coherence time, setting an upper limit on the qubit's operational time as an information carrier and computational unit. Additionally, spin-orbit coupling (SOC) and zero-field splitting (ZFS), govern the spin read-out resonance, spin-initialization process, and optically detected magnetic resonance (ODMR) contrast.

We perform the search for the triplet ground state by screening through the substitution defect element across the periodic table, where the search range for the defects was determined by the transition metal electronegativity and electron counting [23] (More details for the search in SI section I). From this first step we identified four candidates of $(\text{X}_{\text{Zn}}\text{V}_{\text{O}})^q$ (q is the charge state of defect complexes, only zero or positive for n-type defects here), specifically $\text{Ti}_{\text{Zn}}\text{V}_{\text{O}}$, $(\text{V}_{\text{Zn}}\text{V}_{\text{O}})^+$, $(\text{Mo}_{\text{Zn}}\text{V}_{\text{O}})^{2+}$, $(\text{Nb}_{\text{Zn}}\text{V}_{\text{O}})^+$. Among these defects, the corresponding spin-triplet charged states of Ti have been shown to be thermodynamically unstable, as discussed in Section II A, leaving three candidates $((\text{Mo}_{\text{Zn}}\text{V}_{\text{O}})^{2+}$, $(\text{Nb}_{\text{Zn}}\text{V}_{\text{O}})^+$, $(\text{V}_{\text{Zn}}\text{V}_{\text{O}})^+$) for further investigations.

The single-particle diagram and wave functions of the three thermodynamically stable candidates are shown in Figure 2, which are computed using range-separated hybrid function (HSE) with Fock exchange ratio of 0.375

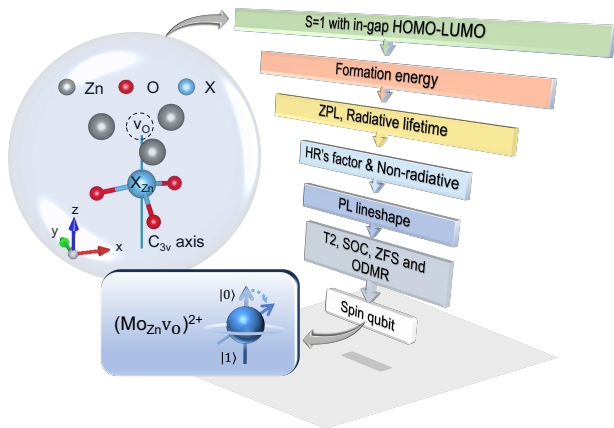


FIG. 1: The computational workflow of defect candidate search with critical parameters.

(More details are in Sec. IV A). All three candidates exhibit a similar origin for their defect-related orbitals, where the $1a_1$ and $2a_1$ states originate from v_O -related states mixed with the d_{z^2} orbital from the transition metal substitution (X_{Zn}). The doubly degenerate $e_{x,y}$ states originate from the d_{xz} and d_{yz} orbitals of the transition metal defect hybridized with the Zn dangling bond from v_O , forming the lowest-energy pair among the five d orbitals split by the C_{3v} crystal field as the detailed molecular orbital diagram shown in SI Figure S2.

While the $e_{x,y}$ orbitals in the spin-majority channel appear within the band gap for $(Mo_{Zn}v_O)^{2+}$ and $(Nb_{Zn}v_O)^+$, their counterparts in the spin-minority channel, as well as in both channels for $(V_{Zn}v_O)^+$, are all located more than 1.5 eV above the conduction band (CB), not visible in Figure 2. This is due to the Hund's Rules, where the electronic filling of the d orbitals always prefer the open shell configurations, and the occupied $e_{x,y}$ orbitals at spin majority channel will have lower in-gap energy levels. Note that the optical transition energies are smaller than the HOMO-LUMO gap in the single particle band structure, because of excited-state reorganization and relaxation.

A. Defect Formation Energy

In Fig. 3 and Table I, we show the defect formation energies and charge transition levels of transition-metal-vacancy complex defects, and intrinsic vacancy defects (v_O and v_{Zn}), at O-poor and O-rich conditions. We note that the charge states $2+$, $1+$, and $1+$ that correspond to the triplet ground state of $Mo_{Zn}v_O$, $Nb_{Zn}v_O$, and $V_{Zn}v_O$, respectively, are stable within the gap. Furthermore, these defects show stable positive charged states for Fermi level positions up to 0.2 eV below the CBM, primarily causing them to act as electron donors.

As shown in Fig. 3 and Table I, the charge transition

level $\epsilon(2+/+)$ for $(Nb_{Zn}v_O)^+$ and $(V_{Zn}v_O)^+$ occurs at 0.79 eV and 1.79 eV below the conduction band minimum (CBM, at 3.43 eV), respectively, and $\epsilon(3+/2+)$ of $(Mo_{Zn}v_O)^{2+}$ is 1.26 eV below the CBM. This makes them the deep donor defects formed in ZnO. On the other hand, the $Ti_{Zn}v_O$ has the $\epsilon(+/0)$ transition at 0.85 eV above the CBM, therefore unlikely to form at the neutral state.

The defect formation energies of all three defects can resemble intrinsic donor v_O [24]. In the n-type region (the Fermi level close to CBM), the proposed defect formation energies are small at O-poor condition and moderately large at O-rich condition, compared to all the other intrinsic defects. It is worth noticing that the intrinsic defects that have a smaller formation energy at the O-rich condition are mostly acceptors (v_{Zn}), meaning that they could compensate the n-type donor defects.

Finally, we discuss our results for the intrinsic defects. On the one side, for v_O , we report the transition level $\epsilon(2+/0)$ to be 2.31 eV above the VBM. Additionally, our calculations indicate an unstable $1+$ charge state, making this defect a negative- U center, consistent with previously reported results obtained using hybrid functionals [25–27]. In the case of v_{Zn} , our results show it to be an amphoteric defect, in which the $2-$, $1-$, $1+$ and $2+$ charges states are stable, which is in agreement with previous studies [26]. Given the abundance of vacancy defect formation in ZnO and their similar formation energies with proposed metal-vacancy defects, we conclude the latter would be able to form in ZnO as well.

B. Optical interface

The control and read-out of deep defect qubits in quantum information applications are typically mediated by spin-photon interfaces. In particular, spin-dependent photoluminescence intensity is directly related to the excited-state kinetics among different spin states, which eventually provides for spin polarization and readout. It is thus essential to investigate the optical properties. In this section, we compute the absorption spectrum, radiative lifetime (τ_R) and zero-phonon line (ZPL) energy. Then we consider the phonon-related properties revealing the characteristics of photoluminescence lineshape.

1. ZPL, absorption spectrum and radiative lifetime

We summarize the optical absorption energy (E_V^{RPA}), radiative lifetime (τ_R), excited-state relaxation energy (E_{rel}), and the zero-phonon lines (ZPL) of the three defects in Table II. Based on the analysis of group theory for C_{3v} and computed absorption spectra, the $e \rightarrow 2a_1$ transition is only allowed when light is polarized in the x-y plane for the majority spin channel, while the $a_1 \rightarrow 2a_1$ transition is only allowed when light is polarized along the z direction for the minority spin channel.

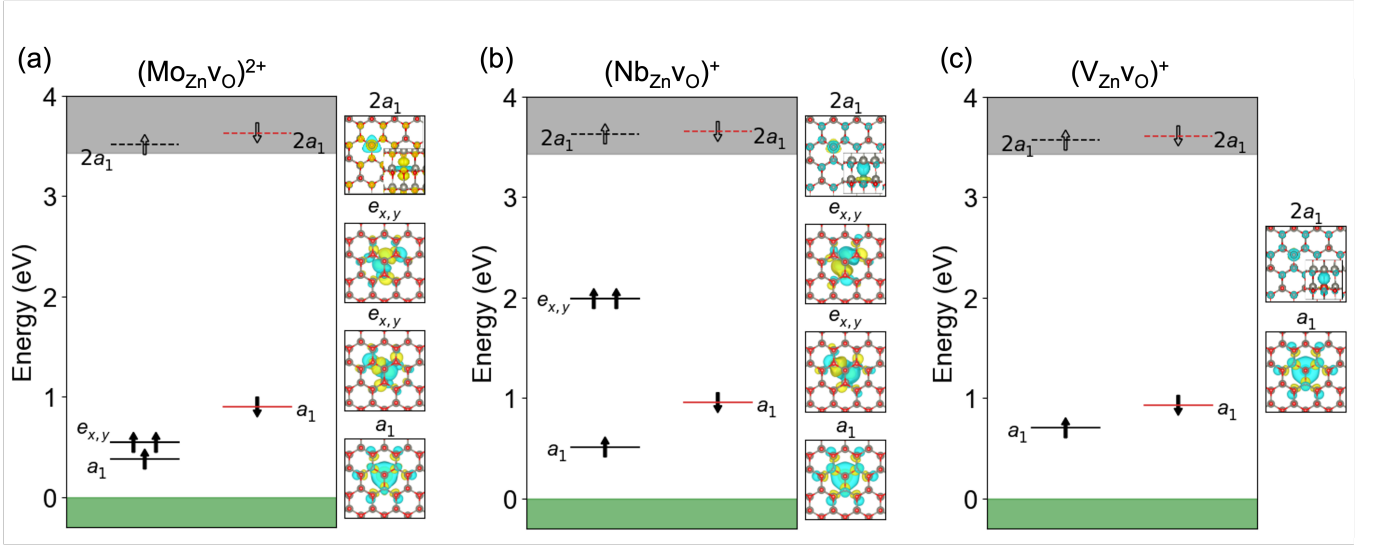


FIG. 2: Single-particle levels and wavefunctions. Single-particle defect levels (horizontal black (majority spin) and red lines (minority spin)) of the (a) $(\text{Mo}_{\text{Zn}}\text{VO})^{2+}$, (b) $(\text{Nb}_{\text{Zn}}\text{VO})^+$, and (c) $(\text{V}_{\text{Zn}}\text{VO})^+$ defects in ZnO, calculated at the HSE ($\alpha=0.375$) level. The green/gray area corresponds to the valence/conduction band of ZnO, respectively. The orbitals labeled with the same symmetry symbol across three defects share the same feature and wave function natures. The quasiparticle band structure of $(\text{Mo}_{\text{Zn}}\text{VO})^{2+}$ and $(\text{Nb}_{\text{Zn}}\text{VO})^+$ in ZnO computed at the GW approximation can be found in SI FIG. S9.

TABLE II: Summary of optical properties of proposed defects. The list includes ZPL energy computed by cDFT (ZPL^{cDFT}), relaxation energy computed by cDFT (E_{rel}), absorption energy computed by RPA ($E_{\text{v}}^{\text{RPA}}$), ZPL energy obtained by RPA absorption energy subtracting the relaxation energy ZPL^{RPA} , module square of the transition dipole moment (μ^2), and radiative lifetime (τ_R) for each ZnO defect system ($(\text{Mo}_{\text{Zn}}\text{VO})^{2+}$, $(\text{Nb}_{\text{Zn}}\text{VO})^+$, $(\text{V}_{\text{Zn}}\text{VO})^+$). The ZPL and τ_R calculations performed at TDDFT and GW-BSE can be found in SI TABLE S7.

Spin	Transition	ZPL^{cDFT} (eV)	E_{rel} (eV)	$E_{\text{v}}^{\text{RPA}}$ (eV)	ZPL^{RPA} (eV)	μ^2 (bohr ²)	τ_R (μs)
$(\text{Mo}_{\text{Zn}}\text{VO})^{2+}$							
Maj	$e \rightarrow a_1$ (x,y)	1.99	0.18	2.96	2.78	7.21×10^{-2}	1.21
Min	$a_1 \rightarrow 2a_1$ (z)	1.56	0.85	2.61	1.76	2.00×10^{-2}	6.38
$(\text{Nb}_{\text{Zn}}\text{VO})^+$							
Maj	$e \rightarrow a_1$ (x,y)	1.07	0.51	1.52	1.01	8.09×10^{-2}	7.92
Min	$a_1 \rightarrow 2a_1$ (z)	1.72	0.74	2.64	1.90	2.82×10^{-2}	4.35
$(\text{V}_{\text{Zn}}\text{VO})^+$							
Maj	$a_1 \rightarrow 2a_1$ (z)	0.13	2.49	2.87	0.38	6.09×10^{-2}	1.55
Min	$a_1 \rightarrow 2a_1$ (z)	1.62	0.86	2.58	1.72	2.19×10^{-3}	59.66

First, we compute the absorption spectrum at the Random-Phase Approximation including local-field effects, with the hybrid functional wavefunction as inputs (RPA@HSE, see Fig. S3 in SI). The absorption energies of the defect transitions are well separated from the excitation of bulk states, ranging from ultra-red to blue. With input of excitation energy and transition dipole moments, we obtain the radiative lifetimes on the microsecond scale, e.g. with the $e \rightarrow 2a_1$ transition in $(\text{Mo}_{\text{Zn}}\text{VO})^{2+}$ the shortest lifetime ($\sim 1.21 \mu\text{s}$). The longest radiative lifetime of $60 \mu\text{s}$ is observed in the spin-

minority transition of $(\text{V}_{\text{Zn}}\text{VO})^+$, where the corresponding peak in the spectrum becomes barely observable (see Fig. S3 in SI). For comparison of other spin defect qubits, the lifetimes of proposed defect candidates are longer than the NV center (12 ns) [28], but shorter than the boron vacancy in hBN ($20 \mu\text{s}$) [29]. The difference is primarily from variation of dipole moments based on Eq. 4, i.e. the NV center has a transition dipole moment ($\mu^2 \sim 3.87$ [30]), much larger than that of our proposed systems ($\mu^2 \sim 10^{-2}$), while the boron vacancy exhibits a much smaller non-zero dipole moment ($\mu^2 \sim 10^{-4}$ [31]).

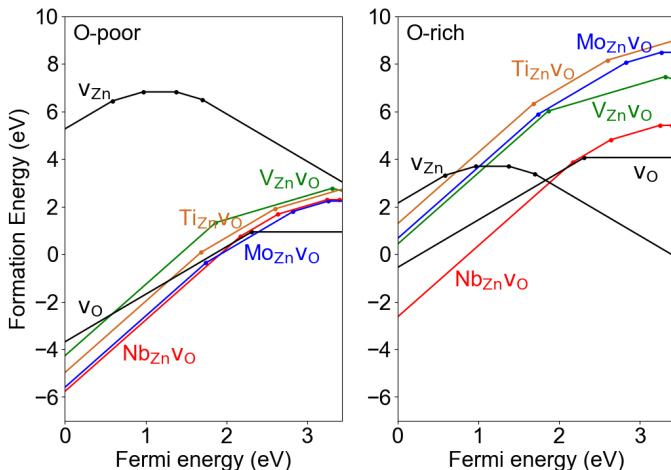


FIG. 3: Formation energies of the complex vacancy defects $X_{\text{Zn}}\text{V}_\text{O}$ ($X=\text{Mo}, \text{Nb}, \text{Ti},$ and V) and intrinsic defects v_O and v_Zn at O-poor(left)/O-rich (right) conditions.

Defect	q/q'	$\varepsilon(q/q')$
$\text{Mo}_{\text{Zn}}\text{V}_\text{O}$	$3+/2+$	1.74
	$2+/1+$	2.82
	$1+/0$	3.26
$\text{Nb}_{\text{Zn}}\text{V}_\text{O}$	$3+/2+$	2.17
	$2+/1+$	2.64
	$1+/0$	3.24
	$0/1-$	3.40
$\text{Ti}_{\text{Zn}}\text{V}_\text{O}$	$3+/2+$	1.68
	$2+/1+$	2.60
$\text{V}_{\text{Zn}}\text{V}_\text{O}$	$3+/1+$	1.87
	$1+/1-$	3.31
v_O	$2+/0$	2.31
v_Zn	$2+/1+$	0.59
	$1+/0$	0.97
	$0/1-$	1.38
	$1-/-2-$	1.70

TABLE I: Calculated charge transition levels $\varepsilon(q/q')$ (in eV) referenced to the VBM. The CBM position is at 3.43 eV.

We next calculate the ZPL energy from two methods, one is from the total energy difference between the excited state and the ground state energy at their equilibrium geometries respectively (ZPL^{cDFT}); another is by subtracting the excited-state relaxation energy from the vertical excitation energy ($\text{ZPL}^{\text{RPA}} = E_v^{\text{RPA}} - E_{\text{rel}}$). Note at the RPA level, the vertical transition energy is very close to the single particle energy difference between states involved in the transition. The ZPLs esti-

ated by both methods are generally consistent if the delocalization error from V_{xc} is small, or equivalently, the exchange-correlation functional satisfies the Koopman's condition [32]. In Table II, we found that in most cases ZPL^{cDFT} and ZPL^{RPA} at the same exchange-correlation functional are mostly consistent, indicating a relatively small delocalization error in our chosen exchange-correlation functional. However, an exception is the spin-majority transition of $(\text{Mo}_{\text{Zn}}\text{V}_\text{O})^{2+}$, where a band inversion occurred between $2a_1$ and $3a_1$ with cDFT, indicating strong reorganization of energy levels not captured by RPA.

Given that cDFT is still at the mean-field level which is lack of many-body effects, we further employ the time-dependent density-functional theory (TDDFT) with hybrid exchange-correlation kernel and many-body perturbation theory (GW-BSE) methods, with starting point single particle states computed at hybrid functional, as shown in SI Fig.S9. We adopted the numerical method without the need of explicit empty-states, as implemented in the WEST code, in order to properly converge the calculations, since ZnO is well known for a difficult case for empty-state convergence previously [33]. We note that the ZPL values between GW-BSE and TDDFT methods are close within 0.2 eV across different transitions. This indicates that TDDFT with hybrid exchange-correlation kernel gives reasonable descriptions of electron-hole interactions. Comparing with cDFT, the values of GW-BSE and TDDFT are generally smaller. Specifically with the case of $(\text{Mo}_{\text{Zn}}\text{V}_\text{O})^{2+}$, the majority spin ZPL energy at BSE is 1.39 eV, compared to CDFE 1.99 eV.

From Table II by CDFT and SI Table xx by GW-BSE, most of the ZPLs are between 1 eV – 2 eV, within the energy range for efficient optical readout, except the spin majority channel transition of $(\text{V}_{\text{Zn}}\text{V}_\text{O})^+$. The band flip was observed to account for the huge excited-state relaxation energy of spin majority channel transition of $(\text{V}_{\text{Zn}}\text{V}_\text{O})^+$, indicating strong electron-phonon coupling. Therefore we exclude it from our promising candidate list. We choose the ZPL^{cDFT} as inputs for calculations in the following sections for the sake of theory consistency among different properties.

For physical implications, the excited-state relaxation energies of the $a_1 \rightarrow 2a_1$ transition are in general larger than the $e \rightarrow a_1$ transition, indicating a stronger electron-phonon coupling. The $a_1 \rightarrow 2a_1$ transition in all three systems originates from the transition observed in v_O defect (see Fig. S2 in SI), which is characterized by a strong electron-phonon coupling and significant lattice relaxation energy (~ 1 eV). Previous studies show that strong electron-phonon coupling causes the photoluminescence (PL) emission line shifts to drop below 1 eV, where the non-radiative recombination dominates over the radiative recombination in the case of v_O [34].

Although single transition metal (TM) substitutions can form triplet ground states, as the case for Mo_{Zn} or Nb_{Zn} with $1e_{x/y} \rightarrow 2e_{x/y}$ transitions, these transitions

are optically-forbidden and have large energy splittings due to Coulomb interactions and strong crystal fields (e.g., 4.5 eV in $\text{Mo}_{\text{Zn}}^{2+}$, exceeding the ZnO band gap). In contrast, TM + vacancy complexes hybridize the d_{z^2} orbitals from the TM with the a_1 states from vacancy dangling bonds, creating a localized $2a_1$ state near the band edge. This hybridization reduces the electron-phonon coupling compared to v_{O} and breaks the selection rule of forbidden $d-d$ transitions, causing the $e \rightarrow a_1$ transition to be stronger and more promising for the optical readout (see Fig. S2 in SI). Therefore, (TM) + vacancy complexes are more favorable candidates for spin qubits than single TM substitutions or single vacancies in ZnO.

2. Huang-Rhys factor

To further characterize the phonon-related optical properties of the defect candidates, we computed the Huang-Rhys (HR) factors [35, 36], non-radiative lifetime (τ_{NR}) [37], as well as the quantum yield, as summarized in Table IV. The HR factor quantifies the strength of electron-phonon coupling and the energy reorganization during electronic transitions. Small electron-phonon coupling strength gives small HR factor (a larger Debye-Waller factor), which is essential for the relative intensity of the ZPL compared to the phonon sideband.

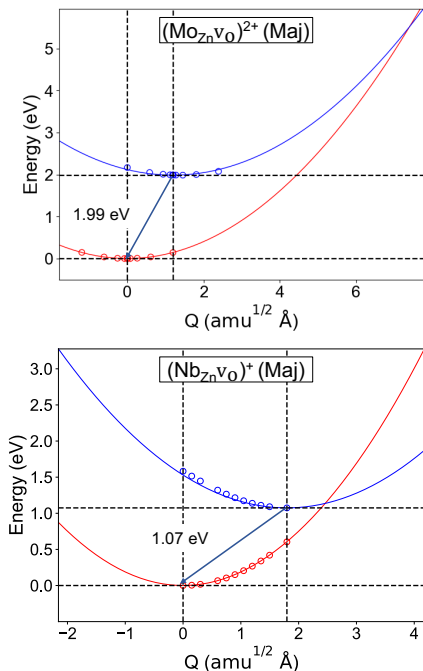


FIG. 4: Configuration coordinate diagram of the potential surface (dots) fitted by harmonic potentials with effective phonon modes (lines). Top panel: $e \rightarrow a_1$ transition in $(\text{Mo}_{\text{Zn}}\text{VO})^{2+}$; bottom panel: $e \rightarrow a_1$ transition in $(\text{Nb}_{\text{Zn}}\text{VO})^+$.

Fig. 4 shows the potential energy surfaces (PES) along

the one-dimensional configuration coordinate by interpolation between the ground state and excited state geometries [35]. The effective phonon energy $\hbar\omega_{eff}$ and the corresponding HR factors are listed in Table S6 in the SI. To compute $\hbar\omega_{eff}$, we considered the harmonic approximation and fitted the PES to $E(Q) = \frac{1}{2} * \omega_{eff}^2 * Q^2$. The HR factor is calculated with an effective phonon S_f^{eff} , approximated by $S = \omega_{eff}\Delta Q^2/2\hbar$ (plotted in Fig. S4 in the SI). The mass-weighted displacements between the excited and ground state geometries is defined as $\Delta Q = \sqrt{\sum_{\alpha,t} m_{\alpha}\Delta R_{\alpha,t}^2}$ [35], where m_{α} is the atomic mass of the atom α , and $R_{\alpha,t}$ is the atomic displacement of atom α at direction t , which can also be interpreted as the effective phonon mode. The Debye-Waller factor, defined as the integrated luminescence intensity of the ZPL, I_{zpl} , divided by the integrated luminescence intensity of the total spectrum, I_{tot} , can be approximately computed as $DW^{eff} = \frac{I_{zpl}}{I_{tot}} = e^{-S_f^{eff}}$ [38]. Additionally, we compared the effective phonon method with summing up all phonon eigenmodes for the HR factor in IIB 4, which show qualitatively good agreement.

TABLE III: A summary of HR factor (S) of various defects from past literature and this work.

Defect(host)	$\Delta Q(\text{amu}^{1/2}\text{\AA})$	$\hbar\omega(\text{meV})$	S
$(\text{Mo}_{\text{Zn}}\text{VO})^{2+}(\text{ZnO})$	1.19	28	4.73
$(\text{Nb}_{\text{Zn}}\text{VO})^+(\text{ZnO})$	1.80	34	13.25
Li_{Zn} [39](ZnO)	3.22	36	28
N_{O} [40](ZnO)	1.92	40	15.3
$\text{Cu}_{\text{Zn}}^{-\rightarrow 0}$ [41](ZnO)	$\approx 1.39^a$	57	13.1
$\text{Cu}_{\text{Zn}}^{+\rightarrow 0}$ [41](ZnO)	$\approx 1.33^a$	52	11.0
$\text{V}_{\text{Zn}}\text{Al}_{\text{Zn}}^{0\rightarrow -}$ [42](ZnO)	2.7	33	25
$\text{V}_{\text{Zn}}\text{Si}_{\text{Zn}}^{+\rightarrow 0}$ [42](ZnO)	2.7	33	25
$\text{V}_{\text{Zn}}\text{H}^{0\rightarrow -}$ [42](ZnO)	2.95	30	27
C_{N} [39](GaN)	1.61	42	10
$\text{Zn}_{\text{Ga}}\text{V}_{\text{N}}$ [39](GaN)	3.33	26	30
NV^- [43](Diamond)	$\approx 0.7^a$	64	3.67
$\text{Cl} - \text{V}$ [44](4H-SiC)	$\approx 0.96^a$	32 to 40	3.55 to 4.43
VB^- [29, 31](hBN)	$\approx 1.1^a$	24.8	3.69
$\text{C}_{\text{B}}\text{C}_{\text{N}}$ [45](hBN)	$\approx 0.38^a$	120	2
$\text{N}_{\text{B}}\text{V}_{\text{N}}$ [46](hBN)	0.66	30,46,48 ^b	4.49

Table III summarizes examples of HR factors for defects in different host materials. First, we found overall host materials with light element (C, BN) have smaller HR factors (e.g. compared to ZnO, GaN). This can be understood by the atomic mass dependence (m) in ΔQ . Next, the dominant phonon frequency has variation within a few times, in particular among defects in ZnO, within a factor of 2. As a result, the major determining factor for the variation of HR in one host materials (e.g. ZnO) can be only from the displacement between the excited and ground states ($\Delta R_{\alpha,t}$), if the number of atoms involved is similar, namely similar real-space localization as an example shown in Fig. 5.

Our proposed $(\text{Mo}_{\text{Zn}}\text{VO})^{2+}$ defect (spin-majority channel $e \rightarrow 1a_1$ transition) has a surprisingly small HR's factor 4.73, which is slightly larger than NV center in diamond, but one of the smallest among known defects in ZnO. Furthermore, experiments have been able to optically resolve the zero phonon line (ZPL) of copper defects, which have a HR factor of 11 [41]. This suggests that the zero-phonon line of $(\text{Mo}_{\text{Zn}}\text{VO})^{2+}$ should be able to resolve as well (given the transition being optically allowed), which will be discussed in detail in section II B 4 and Figure 6.

In order to understand why $(\text{Mo}_{\text{Zn}}\text{VO})^{2+}$ defect has a smaller HR factor than other defects in ZnO, we compare $(\text{Mo}_{\text{Zn}}\text{VO})^{2+}$ and $(\text{Nb}_{\text{Zn}}\text{VO})^+$ as an example. In Fig. 5, we show the effective phonon mode and the contribution to ΔQ^2 from atoms in real space for the spin majority transition of $(\text{Mo}_{\text{Zn}}\text{VO})^{2+}$ and $(\text{Nb}_{\text{Zn}}\text{VO})^+$. Both of the two systems have an effective phonon mode localized within 5 Å from the TM defect center. The major contributors to ΔQ^2 arise from the Zn atoms around the vacancy and next-nearest neighbors of the TM substitution site. With similar atomic mass contributions (single atom Mo or Nb mass difference is negligible in the summation), the smaller ΔQ^2 of $(\text{Mo}_{\text{Zn}}\text{VO})^{2+}$ is mostly from overall smaller atomic displacement (ΔR_α) between ground and excited states, which is also consistent with the smaller excited-state relaxation energy E_{rel} (0.18 eV) compared to $(\text{Nb}_{\text{Zn}}\text{VO})^+$ (0.51 eV) in Table II.

3. Non-radiative recombination

Non-radiative (NR) recombination refers to electron-hole recombination mediated by phonons, which does not contribute to photoluminescence. The optical brightness, determined by the competition between radiative and non-radiative recombination paths, is characterized by the quantum yield ($\text{QY} = \frac{1/\tau_R}{1/\tau_R + 1/\tau_{NR}}$). As shown in Table IV, we found that the spin-majority NR transition in $(\text{Mo}_{\text{Zn}}\text{VO})^{2+}$ and the spin-minority NR transition in $(\text{Nb}_{\text{Zn}}\text{VO})^+$ are forbidden. Intuitively, the non-radiative recombination process can be understood from the classical Marcus theory (i.e. the high temperature limit), as illustrated in Figure 4. The potential energy surface crossing between the ground state (red curve) and the excited state (blue curve) defines an energy barrier which the phonon-assisted non-radiative recombination process needs to overcome.

From a theoretical perspective, the phonon-assisted non-radiative recombination rate, within the static coupling approximation and the one-dimensional effective phonon approximation, is proportional to the product of two terms: the square of electronic term (W_{if}) and the phonon term (χ_{if}) [37]. The electronic coupling term exhibits relatively small variation between two defects as shown in Table IV.

The non-radiative lifetimes of the spin-majority transition $e \rightarrow 2a_1$ of $(\text{Mo}_{\text{Zn}}\text{VO})^{2+}$ and $(\text{Nb}_{\text{Zn}}\text{VO})^+$ differ signif-

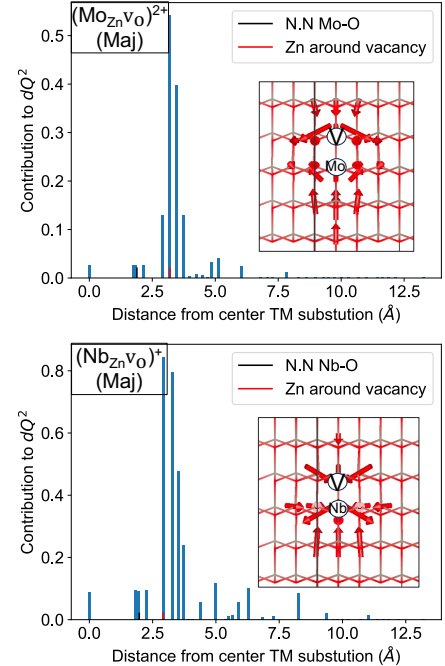


FIG. 5: The module square of mass weighted displacement dQ^2 distribution for proposed defects. dQ^2 for the spin-majority transition of $(\text{Mo}_{\text{Zn}}\text{VO})^{2+}$ (top) and $(\text{Nb}_{\text{Zn}}\text{VO})^+$ (bottom) contributed from atoms at radius r Å from the TM defect center. The contribution to dQ^2 from atom at r Å from the TM site, defined as $dQ^2(r) = \sum_{\alpha} dQ^2(\alpha)|_{|r_{\alpha}-r|<0.1}$, where the r_{α} is the atom α 's distance from TM site and 0.1 is the step size of the sampling. The total displacement $\Delta Q = \int dQ^2(|\vec{r}|)d\vec{r}$.

icantly. Qualitatively, a much larger barrier is obtained in $(\text{Mo}_{\text{Zn}}\text{VO})^{2+}$ than $(\text{Nb}_{\text{Zn}}\text{VO})^+$ as shown in Fig. 4, which results in much slower non-radiative process in $(\text{Mo}_{\text{Zn}}\text{VO})^{2+}$. This could be understood from a much larger ZPL and smaller ΔQ in $(\text{Mo}_{\text{Zn}}\text{VO})^{2+}$. Furthermore, the major contribution to the difference arises from χ_{if} , as can be seen from our results, the phonon term of $(\text{Nb}_{\text{Zn}}\text{VO})^+$ is many orders of magnitude larger than that of $(\text{Mo}_{\text{Zn}}\text{VO})^{2+}$. Consequently, $(\text{Nb}_{\text{Zn}}\text{VO})^+$ exhibits stronger electron-phonon coupling, leading to a faster non-radiative decay. More detailed discussion can be found in SI Figure S7.

Additionally, to test the dependence of non-radiative lifetime and QY on the chosen electronic structure theory, we calculate the non-radiative lifetime using the ZPL values obtained from GW-BSE and TDDFT while using the cDFT phonons and electronic wavefunctions. Similar conclusions remain for the quantum yield of the spin majority and minority channels of $(\text{Mo}_{\text{Zn}}\text{VO})^{2+}$, as shown in Table S7 in the SI.

TABLE IV: The phonon-related properties of optical spectroscopy for $(\text{Mo}_{\text{Zn}}\text{VO})^{2+}$ and $(\text{Nb}_{\text{Zn}}\text{VO})^+$. $\hbar\omega_{eff}$ (gs/es) is effective phonon energy of excited state and ground state, and factor $k \approx \frac{ZPL}{\hbar\omega_{eff}(gs)}$ are used to approximate the number of phonons needed to mediate the transition. S_f^{eff} (gs/es) are the HR's factor computed by effective phonons for ground state and excited state. τ_{NR} is the non-radiative lifetime. W_{if} and χ_{if} are the electronic part and phonon part of the nonradiative lifetime (τ_{NR}). QY is the Quantum Yield. ΔQ is the mass-weighted displacements between the excited and ground state geometries, as part of entry in S .

Spin	Transition	ZPL (eV)	ΔQ (amu ^{1/2} Å)	k	τ_{NR} (μs)	W_{if} (eV/(amu ^{1/2} Å))	χ_{if}	S_f^{eff} (gs/es)	QY
$(\text{Mo}_{\text{Zn}}\text{VO})^{2+}$									
Maj	$e \rightarrow 1a_1$ (x,y)	1.99	1.19	69	Not allowed	5.13×10^{-2}	1.64×10^{-29}	4.96/4.73	High (≈ 1)
Min	$1a_1 \rightarrow 2a_1$ (z)	1.56	5.05	94	1.08×10^{-7}	3.75×10^{-2}	2.31×10^{-1}	50.64/52.22	Small (≈ 0)
$(\text{Nb}_{\text{Zn}}\text{VO})^+$									
Maj	$e \rightarrow 1a_1$ (x,y)	1.07	1.80	27	1.41×10^{-8}	4.42×10^{-2}	1.26	15.31/13.25	Small (≈ 0)
Min	$1a_1 \rightarrow 2a_1$ (z)	1.72	3.83	104	3.05×10^{-5}	4.62×10^{-2}	5.36×10^{-4}	35.67/35.72	Small (≈ 0)

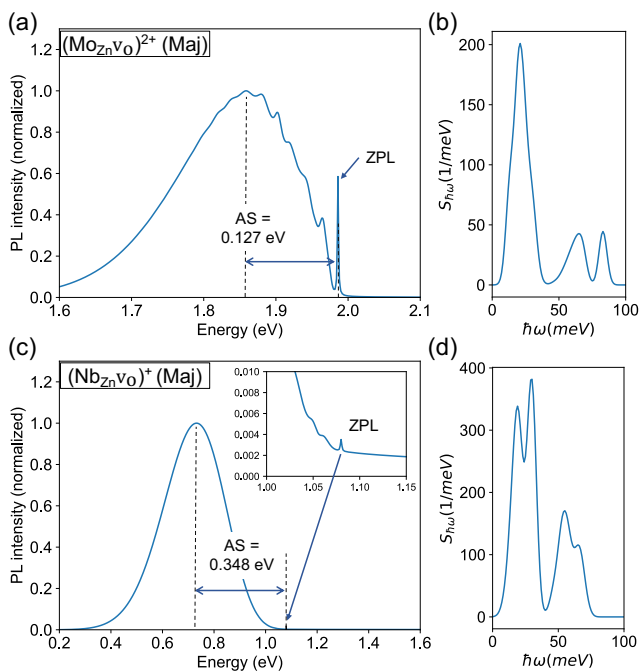


FIG. 6: The photoluminescence(PL) lineshape and partial HR factors. (a) PL lineshape for the spin-majority channel $e \rightarrow 2a_1$ transition of (a) $(\text{Mo}_{\text{Zn}}\text{VO})^{2+}$ and (c) $(\text{Nb}_{\text{Zn}}\text{VO})^+$. The anti-stoke shift(AS) in (a) and (c) is determined by the energy difference between the highest peak of phonon side band (PSB) and the ZPL. The corresponding phonon spectrum function in (b) and (d) reveal the partial HR factor contributed by the phonon mode with energy $\hbar\omega$.

4. Photoluminescence Lineshape

We next discuss the photoluminescence (PL) lineshape and phonon sidebands of the $(\text{Mo}_{\text{Zn}}\text{VO})^{2+}$ and

$(\text{Nb}_{\text{Zn}}\text{VO})^+$. Between two spin channels, spin-majority transitions corresponding to the $(e \rightarrow 2a_1)$ transition, can give a distinguishable ZPL peak, as shown in Figure 6. On the other hand, the spin-minority transitions both have large phonon sideband and anti-Stokes (AS) shift (See SI Figure S9). Between the two defects, the $(\text{Mo}_{\text{Zn}}\text{VO})^{2+}$ exhibits a sharp and bright ZPL peak and a phonon side band with an AS shift of 0.127 eV. While the ZPL of $(\text{Nb}_{\text{Zn}}\text{VO})^+$ is relatively small, the AS of 0.348 eV allow it to be distinguishable from the large PSB.

In the Franck-Condon picture, the AS shift corresponds to the ground state energy difference between its equilibrium geometry and excited-state geometry. We found its values (0.13 eV for $(\text{Mo}_{\text{Zn}}\text{VO})^{2+}$ and 0.35 eV for $(\text{Nb}_{\text{Zn}}\text{VO})^+$) are close to the values from CDFT relaxation energy of ground state, i.e. 0.14 for $(\text{Mo}_{\text{Zn}}\text{VO})^{2+}$ and 0.50 eV for $(\text{Nb}_{\text{Zn}}\text{VO})^+$, respectively. Furthermore, by summing up the partial HR factor contributions from each phonon mode, we obtained the HR factors of 4.13 for $(\text{Mo}_{\text{Zn}}\text{VO})^{2+}$ and 10.41 for $(\text{Nb}_{\text{Zn}}\text{VO})^+$. These values are qualitatively consistent with those calculated using the effective phonon approximation, which are 4.73 and 13.25, respectively (see Table IV). The agreement above validates the consistency between different theoretical approaches i.e. using all phonon eigenmodes and effective phonon along the configuration coordinate for phonon-assisted electronic transitions.

The corresponding partial HR factor spectrum functions are shown in Fig. 6 (c, d). We found $(\text{Mo}_{\text{Zn}}\text{VO})^{2+}$ has a dominant peak at 21 meV, and $(\text{Nb}_{\text{Zn}}\text{VO})^+$ between 19-30 meV and 55-65 meV. To understand the localization of each phonon mode, we compute the inverse participation ratio (IPR), estimating the number of atoms involved in the vibration of phonon mode [47]. We found the IPRs are all larger than 20 for two defects, representing delocalized bulk-like phonon modes. Their energies lie within the acoustic band of bulk ZnO. More details can be found in SI Sec.VIII. At the end, the smaller ab-

solute value of partial HR factor across different energies for $(\text{Mo}_{\text{Zn}}\text{VO})^{2+}$ than $(\text{Nb}_{\text{Zn}}\text{VO})^+$ is responsible for smaller HR factor and larger QY in $(\text{Mo}_{\text{Zn}}\text{VO})^{2+}$ than $(\text{Nb}_{\text{Zn}}\text{VO})^+$ (More details can be found in SI Sec.VIII).

Overall, the comprehensive analysis of the thermodynamic properties, optical properties and electron-phonon coupling of these transition metal vacancy complexes in ZnO demonstrated their suitability for quantum technologies, with $(\text{Mo}_{\text{Zn}}\text{VO})^{2+}$ standing out due to its low formation energy and optimal combination of ZPL energy, radiative lifetime, and electron-phonon coupling characteristics.

C. Spin and Spin-Orbit Properties

1. Spin decoherence time

In order to predict the spin decoherence of the qubit candidates, we first compute their free-induction decay (FID) signals, originating from the random distribution of the Overhauser field due to the hyperfine coupling with the nearby nuclear spins derived from the spinful isotopes of ^{67}Zn ($I=5/2$, 4.1%) and ^{17}O ($I=5/2$, 0.038%). Fig.7(a) and (b) present the FID signals of the $(\text{Nb}_{\text{Zn}}\text{VO})^+$ spin and $(\text{Mo}_{\text{Zn}}\text{VO})^{2+}$ spin, respectively, under three different external magnetic field strengths. We observe that the FID signals are well saturated over the 300 G magnetic field strength, reaching their maximum decay time (T_2^*) to be $0.40 \mu\text{s}$ and $0.37 \mu\text{s}$ for $(\text{Mo}_{\text{Zn}}\text{VO})^{2+}$ and $(\text{Nb}_{\text{Zn}}\text{VO})^+$, respectively. We also find that the FID signal has strong non-Gaussian features with a stretched exponent to be 0.51 and 0.56 for $(\text{Mo}_{\text{Zn}}\text{VO})^{2+}$ and $(\text{Nb}_{\text{Zn}}\text{VO})^+$, respectively, owing to a strong anisotropic nature of the hyperfine coupling [48]. We remark that the T_2^* times of the qubit candidates are an order of magnitude smaller than that of diamond NV centers [49] and spin of a silicon vacancy in SiC [50] due to a large Overhauser field fluctuation induced by the larger magnetic moment of the ^{67}Zn nuclear spin and its higher abundance than those of the ^{13}C nuclear spin (1.1 %) in diamond.

The inhomogeneous broadening effect in FID can be removed by applying the Hahn-echo pulse sequence. Fig.7 (c) and (d) show the computed Hahn-echo signals of the Nb-vacancy and Mo-vacancy, respectively, under three different magnetic field strengths. Notably, we observe that the decoherence occurs at two different time scales: early partial collapse within a μs time-scale followed by a gradual decay over millisecond timescale. The gradual coherence decay is due to the dynamical fluctuation of the nuclear spin bath arising from the magnetic dipolar coupling between nuclear spins [48]. We find that the gradual coherence decay following the early partial collapse is well saturated above the magnetic field of 300 G and it is described by a stretched exponential function with the exponent to be 2.49 (2.32) and the T_2 time to be 4.04 (3.96) ms for $(\text{Mo}_{\text{Zn}}\text{VO})^{2+}$ ($(\text{Nb}_{\text{Zn}}\text{VO})^+$) complex.

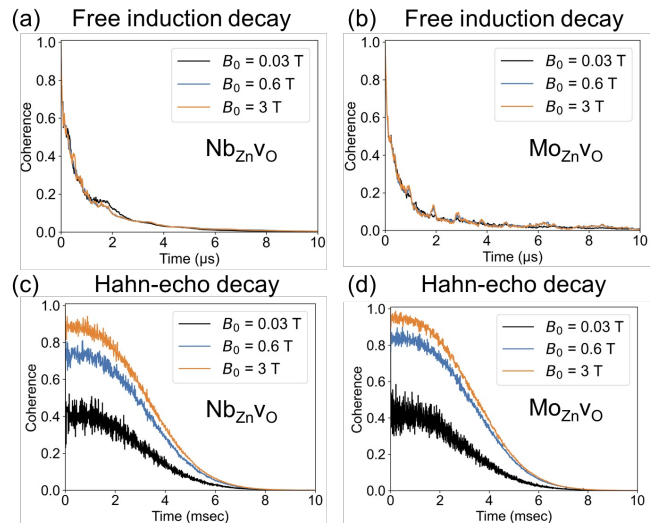


FIG. 7: Spin decoherence of transition metal-vacancy complex in a nuclear spin bath ZnO. (a, b) Free induction decay of $(\text{Nb}_{\text{Zn}}\text{VO})^+$ (a) and $(\text{Mo}_{\text{Zn}}\text{VO})^{2+}$ (b) in ZnO under various external magnetic field strengths (B_0). (c, d) Hahn-echo coherence decay of $(\text{Nb}_{\text{Zn}}\text{VO})^+$ (c) and $(\text{Mo}_{\text{Zn}}\text{VO})^{2+}$ (d) in ZnO under various external magnetic field strengths.

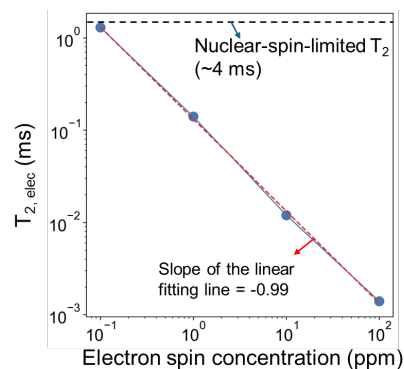


FIG. 8: Electronic spin-induced decoherence time T_2 as a function of the electron spin concentration. The black dotted line shows the T_2 time determined by the nuclear spin bath in ZnO and the red dotted line represents a linear fitting model in logarithmic scale.

We note that the gradual coherence decay is saturated above 300 G as the single-nuclear spin flips or pair-spin flips other than the nuclear spin flip-flop transitions in the bath are suppressed due to large energy gaps between the nuclear spin levels in the bath induced by the Zeeman effect [48].

For the early partial collapse shown in Fig.7 (c) and (d), we find that strain-induced inhomogeneous quadrupole interactions around the defect site (see Supplementary Table 1) are key to understand their origin. The variation of the quadrupole interaction around the

defect leads to varied precession frequencies of the nuclear spins [51], giving rise to irregular electron spin echo envelop modulation (ESEEM) [52–54]. In Supplementary Figure 2, we show that such early coherence collapse vanishes in a hypothetical bath model, for which the quadrupole interaction is removed from the spin Hamiltonian, which confirms the early collapse of the coherence being rooted in the quadrupole interaction. We also find that the partial coherence collapse vanishes by increasing the external magnetic field strength above 3 T as the Larmor frequency becomes the dominant and common frequency of the nuclear spins and the ESEEM depth is suppressed.

In addition to the nuclear spins, ZnO include intrinsic defects and some of them could be paramagnetic [55–58], which could exist even in isotopically purified materials. In such isotopically engineered samples, in which the nuclear spins are removed, the qubit decoherence would be dominated by the electron spin bath due to the paramagnetic defects. To quantitatively predict this effect, we compute the Hahn-echo T_2 time as a function of the concentration of electron spin-1/2 in the ZnO lattice from 0.1 ppm to 100 ppm ($10^{16} - 10^{19} \text{ cm}^{-3}$), which are comparable to the experimental defect concentrations in ZnO [59, 60]. We show in Fig.8 that if the electron spin concentration is 0.035 ppm ($2.85 \times 10^{15} \text{ cm}^{-3}$), the T_2 time induced by the electronic spin bath becomes similar to that of the T_2 time induced by the nuclear spin bath. Our results implies that to benefit from the isotopic purification the paramagnetic defect concentration should be kept under 0.035ppm.

As the electronic spin concentration increases beyond 10^{16} cm^{-3} , the T_2 time is rapidly reduced to sub-millisecond. We find that the T_2 time decreases almost linearly in the log scale with a slope of -0.99. We note that nuclear spins can be removed or significant reduced by nuclear spin purification, then the paramagnetic impurities would be the main source for spin decoherence.

2. Spin-orbit properties and ODMR contrast

In this section, we compute the Zero-Field Splitting (ZFS) and spin-orbit coupling (SOC) of the $(\text{Mo}_{\text{Zn}}\text{VO})^{2+}$ defect. The ground state results, combined with the excited-state calculations from the previous sections, demonstrate that the spin multiplet structure closely resembles that of the NV center. We then perform ODMR simulations, which reveal that a high ODMR contrast can be achieved for spin-based quantum sensing at finite magnetic fields. Finally, leveraging the intrinsic properties of the $(\text{Mo}_{\text{Zn}}\text{VO})^{2+}$ defect, we propose a spin qubit protocol for efficient spin initialization and readout.

Figure 9(a) gives the multiplet structure diagram of $(\text{Mo}_{\text{Zn}}\text{VO})^{2+}$ in ZnO that consists of a triplet ground state, triplet excited state, and two singlet shelving state. This 4-level structure is exactly the same as the NV^{-1} in diamond in the sense of symmetry [61]. This re-

sult is expected because the irreducible representation of the HOMO and LUMO for $(\text{Mo}_{\text{Zn}}\text{VO})^{2+}$ (e and a_1 , respectively) is the same as NV center. The main difference is we found the majority spin transition responsible for the first spin-conserving transition in $(\text{Mo}_{\text{Zn}}\text{VO})^{2+}$ ($e \uparrow \rightarrow a_1 \uparrow$), but the minority spin transition responsible for NV ($a_1 \downarrow \rightarrow e \downarrow$). All excitation energies are obtained from cDFT calculation, except the singlet excitation energy (Δ_{ES}) is obtained by spin-flip TDDFT due to its multi-reference nature.

The degeneracy of the spin triplet manifold is split by intrinsic spin-spin and spin-orbit interactions. This splitting is characterized by the axial ZFS parameter D (between $|m_s = 0\rangle$ and $|m_s = \pm 1\rangle$) and rhombic E (between $|m_s = +1\rangle$ and $|m_s = -1\rangle$). E is zero at C_{3v} symmetry. We obtain a spin-spin contribution [62, 63] $D_{SS} = 4.7$ GHz and spin-orbit contribution [64] $D_{SOC} = -35.6$ GHz, respectively. As a reference, we have obtained the $D_{SOC} + D_{SS} = 21.00$ GHz for the $(\text{V}_{\text{Zn}}\text{VO})^+$, which is in a reasonably good agreement with experiment value of V^{3+} in ZnO, 22.37 GHz [65, 66] (See SI section X).

The spin-orbit coupling is caused by the relativistic effect which couples the electron's spin and orbital motion. The SOC parameters can be used to determine the fine structure of the state and the spin selectivity of optical transitions [67]. At the C_{3v} symmetry, the spin-orbit coupling Hamiltonian can be written in terms of its axial (λ_z) and nonaxial (λ_{\perp}) components:

$$H_{soc} = \lambda_{\perp}/2(L_+S_- + L_-S_+) + \lambda_z L_z S_z \quad (1)$$

where L_{\pm}, L_z and S_{\pm}, S_z are the ladder operators of orbital and spin angular momentum, respectively, in the two-electron spin system in the $|S, m\rangle$ basis.

The SOC matrix elements, λ_z and λ_{\perp} , can mix the spin sub-levels and mediate spin-selective inter-system crossings between different spin sub-levels of the triplet state and the singlet shelving state. The non-radiative inter-system crossing (ISC) rates k between the i, j states can be derived by the Fermi's Golden rule and computed by $k_{ij} = 4\pi\hbar\lambda^2 \tilde{X}_{ij}$, where λ is the SOC coupling parameter defined above and \tilde{X}_{ij} is the phonon coupling term [62]. The non-axial component λ_{\perp} is associated with the transitions between the triplet $m = \pm 1$ spin sub-levels and the singlet level. The axial component λ_z is associated with the transitions between the triplet $m = 0$ spin sub-levels and the singlet level.

We calculate the SOC matrix elements between triplets and singlets at complete active space self-consistent field (CASSCF). This level of theory is necessary because of the multi-reference character of excited-state singlet states [30]. The non-axial component $\lambda_{\perp}({}^3E \rightarrow {}^1A_1)$ is 450 GHz and $\lambda_{\perp}({}^1E \rightarrow {}^3A_2)$ is 3668 GHz. This large SOC originates from the transition metal ion Mo^{4+} in the defect complex, for which, as a reference, the free ion spin-orbit coupling parameter λ is 12741 GHz (defined as $H_{soc} = \lambda \mathbf{L} \cdot \mathbf{S}$ in single atom model with spherical symmetry) [68]. As the ISC rate is proportional

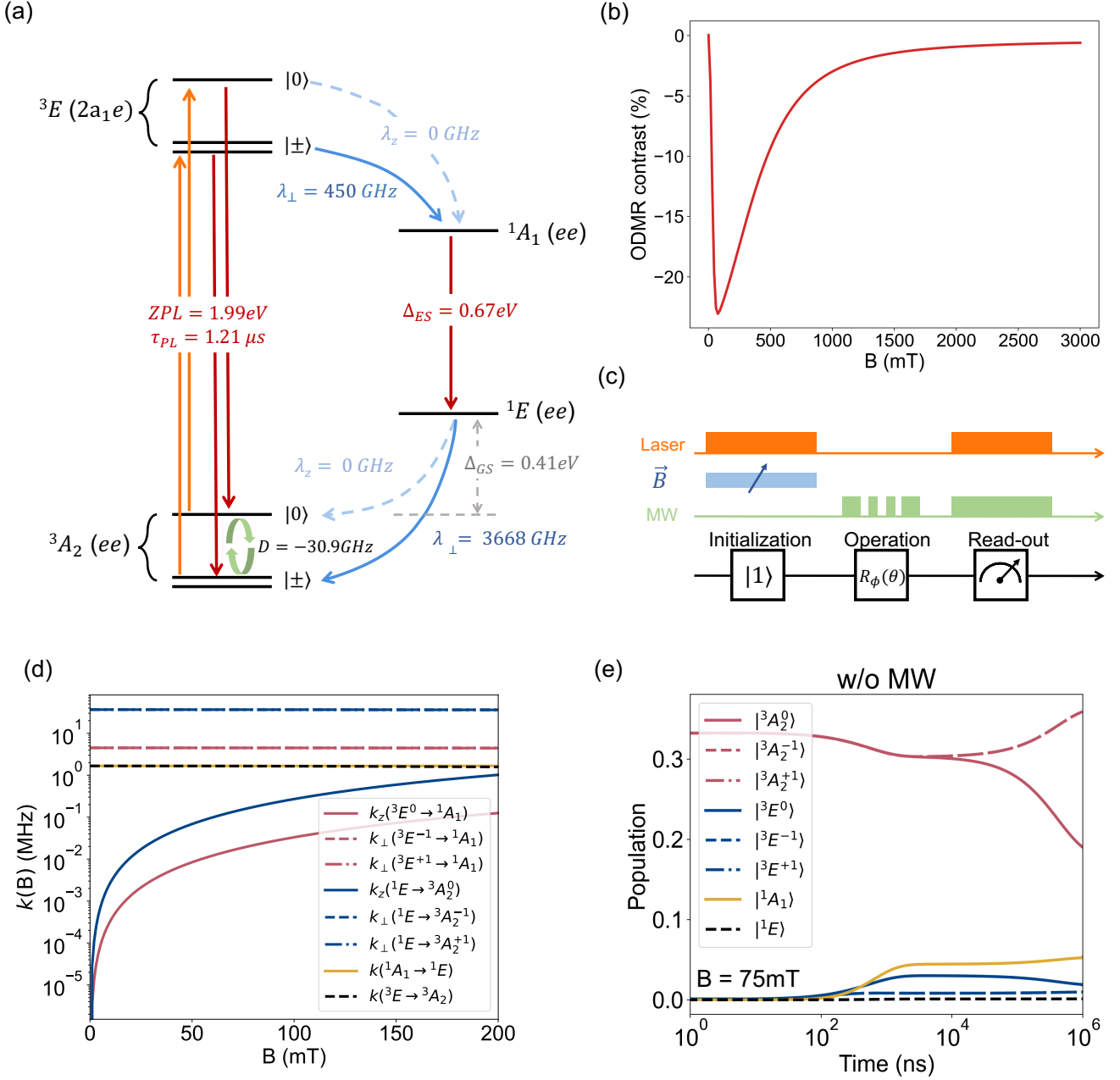


FIG. 9: ODMR simulations and magnetic field dependence. (a) The energy diagram of the $(\text{MoZnVO})^{2+}$. The orange lines denote the spin-conserved optical excitation from ground state triplet to excited state triplet (spin majority channel transition). The red lines denote the spin-conserved radiative/non-radiative recombinations, where the radiative PL lifetime is defined by $\tau_{PL} = 1/(\frac{1}{\tau_R} + \frac{1}{\tau_{NR}})$. The blue lines denote the inter-system crossing process, where the spin-selectivity of this process is determined by the spin-orbit coupling parameter. All the energies in the diagram are obtained by the cDFT, except the singlet excitation energy Δ_{ES} is obtained from spin-flip TDDFT, due to the strong multi-reference nature of the excited-state singlet. (b) is the ODMR contrast dependence on the magnetic field. (c) demonstrates the 3 steps of quantum computing using the spin defect qubit, where the laser, magnetic field, and microwave conditions are denoted for each step. (d) is the magnetic field dependent transition rate k between the two states indicated in parentheses. The left superscript of the state represents the spin multiplicity $(2S+1)$, and the right superscript denotes the spin sub-level (m_s) . (e) The electron population evolved with time at $B=75\text{mT}$ with no microwave applied.

to the square of SOC matrix element, the large SOC likely leads to fast ISC transitions [30]. The axial components $\lambda_z(^3E \rightarrow ^1A_1)$ and $\lambda_z(^1E \rightarrow ^3A_2)$, on the other hand, are found to be zero, consistent with the predictions of group theory for the C_{3v} symmetry [69, 70]. As a comparison, the corresponding SOC parameters in NV center are one order smaller than $(\text{Mo}_{\text{Zn}}\text{VO})^{2+}$: with $\lambda_{\perp}(^3E \rightarrow ^1A_1)=3.9$ GHz and $\lambda_{\perp}(^1E \rightarrow ^3A_2)=5.22$ GHz [30]. This indicates the ISC in $(\text{Mo}_{\text{Zn}}\text{VO})^{2+}$ could be faster than NV center in the diamond. We note that in subsequent simulations we take axial SOC λ_z being zero based on our calculations and group theory.

Using the calculated inputs above, we perform ODMR simulations. More details of ODMR simulation can be found in SI section XII. At room temperature, the thermal fluctuation energy $k_B T = 6.3$ THz significantly exceeds the zero-field splitting (ZFS) of the $(\text{Mo}_{\text{Zn}}\text{VO})^{2+}$ defect, leading to an approximately equal population distribution among the $m_s = 0$, $m_s = 1$, and $m_s = -1$ spin sub-levels. Our simulation assumes an initial thermal equilibrium population.

The ODMR contrast is shown in Figure 9(b). At zero magnetic field ($B = 0$), the contrast is zero at room temperature because the electrons remain locked in their initial spin states due to the absence of allowed axial transitions; the population remains at thermal equilibrium. When a microwave field is applied, it cyclically redistributes the electron population among the spin sub-levels, ultimately leading to an equally distributed populations. As a result, the final spin population mirrors the initial thermal equilibrium distribution. We emphasize that, the ODMR contrast at $B = 0$ is highly dependent on the degree of spin polarization in the initial population—higher polarization enhances the ODMR contrast. We also note that due to non-zero ZFS, at low temperature, the thermal equilibrium among three sublevels would be different, then we should see a small ODMR contrast at $B = 0$. (See additional simulations in the Supplementary Information).

At finite magnetic field ($B > 0$), the absolute ODMR contrast increases and reaches a maximum of 23% at $B = 75$ mT. This enhancement arises from the activation of the spin polarization process due to a nonzero axial ISC rate. The spin population with microwave application remains close to thermal equilibrium (see Supplementary Information), meaning that the ODMR contrast is primarily determined by the spin polarization in the absence of microwave excitation. As illustrated in Figure 9(d), at nonzero magnetic fields, the ISC rate $k_z(^3E \rightarrow ^1A_1)$ becomes nonzero due to spin sub-level mixing. This enables electrons in the $|m_s = 0\rangle$ state to enter the ISC loop, where they preferentially transition to the $^1E |m_s = \pm 1\rangle$ sub-levels due to the large ratio of non-axial to axial transition rates, $k_{\perp}(^1E \rightarrow ^3A_2)/k_z(^1E \rightarrow ^3A_2)$. Consequently, after several optical cycles, the electron population becomes polarized with higher population in the $|m_s = \pm 1\rangle$ sub-levels, as depicted in Figure 9(e). However, at excessively high magnetic fields (Figure 9b), this

transition ratio is significantly reduced, leading to diminished spin polarization, resulting in zero ODMR contrast as shown in the Figure 9(b). From a applications perspective, an $(\text{Mo}_{\text{Zn}}\text{VO})^{2+}$ -based sensor should operate in an applied bias field to enhance ODMR contrast and thus sensitivity.

We noted that in the presence of pseudo Jahn-Teller (PJT) effect, the axial component $k_z(^3E \rightarrow ^1A_1)$ and $k_z(^1E \rightarrow ^3A_2)$ can become non-zero even without the magnetic field, due phonon-mediated state mixing [71–73]. However, previous theory has predicted that the interplay between strong SOC and JT effect can cause the quenched JT distortion in the d^2 electron configuration system [74]. If λ_z remains 0, this opens the path toward highly cyclic transition that can be leveraged for single shot readout at low temperature for quantum information applications. While it is beyond the theory of this work, we expect the ZFS of the the ground state and excited state manifolds to be different due to their different electronic configuration and exchange energy. At low temperature, we can utilize the the ZPL for selective excitation of the $m_s=0$ state. Because of the zero ISC for this state, an unlimited number of optical cycles can be used to determine the spin state. Initialization can also be performed by Radio frequency (RF) manipulation after the spin state is determined.

III. SUMMARY

In this work, we conducted a systematic search of optically-addressable deep point defects promising as spin qubits for quantum information science and technology (QIST), among a group of transition metal-vacancy complexes in ZnO. Our screening process began by identifying defects with a high-spin ground state and subsequently narrowing down the candidates based on thermodynamic stability, allowed optical transitions, and sharp ZPL in photoluminescence (PL). Among the identified candidates, we found that $(\text{Mo}_{\text{Zn}}\text{VO})^{2+}$ exhibits a high-spin ground state ($S=1$), high quantum yield, a sufficiently low Huang-Rhys factor of approximately 4.9, and a sharp zero-phonon line (ZPL) in its PL spectrum. These properties make $(\text{Mo}_{\text{Zn}}\text{VO})^{2+}$ a promising candidate for spin qubit applications.

We investigated the spin decoherence time of the $(\text{Nb}_{\text{Zn}}\text{VO})^+$ and $(\text{Mo}_{\text{Zn}}\text{VO})^{2+}$. The simulation of Hahn-echo experiments demonstrate a two-stage coherence decay process: an early partial collapse driven by strain-induced quadrupole interactions, followed by a gradual decay dominated by nuclear spin dynamics. These defects exhibit robust coherence properties under Hahn-echo measurements, with T_2 times reaching 4.04 ms for $(\text{Mo}_{\text{Zn}}\text{VO})^{2+}$ and 3.96 ms for $(\text{Nb}_{\text{Zn}}\text{VO})^+$ at magnetic fields above 300 G. In addition, our study of electronic spin-induced decoherence in ZnO reveals a critical transition in the spin decoherence mechanism, shifting from nuclear spin-induced to electronic spin-induced spin de-

coherence. We show that paramagnetic defects could fundamentally limit qubit coherence, with electronic spins emerging as the dominant decoherence source at the electronic spin concentration exceeding 0.035 ppm ($2.85 \times 10^{15} \text{ cm}^{-3}$).

Finally, we investigate the spin-orbit coupling (SOC) and zero-field splitting (ZFS) of the $(\text{Mo}_{\text{Zn}}\text{V}_{\text{O}})^{2+}$ defect in ZnO, along with its optically detected magnetic resonance (ODMR) and spin-initialization mechanisms. The $(\text{Mo}_{\text{Zn}}\text{V}_{\text{O}})^{2+}$ defect exhibits a triplet ground state with sizable ZFS. The symmetry and excited state diagram closely resembling the NV^- center in diamond, in absence of its pseudo-Jahn Teller distortion. We demonstrate that a large ODMR contrast can be achieved through magnetic field tuning, enabling precise optical readout and efficient spin polarization. At zero magnetic field, the ODMR signal depends on the initial spin population, allowing for effective optical readout of quantum information. Based on these findings, we developed a spin qubit operation protocol specifically designed for defects with strong spin-orbit coupling and forbidden axial ISC transitions.

In conclusion, the $(\text{Mo}_{\text{Zn}}\text{V}_{\text{O}})^{2+}$ defect in ZnO emerges as a strong candidate for spin qubits for quantum information applications. Its optical and spin properties are comparable to NV, but it has larger zero-field splitting and stronger spin-orbit coupling for intersystem crossing. This may enhance spin-information fidelity, highlighting its suitability for high-precision quantum technologies.

IV. COMPUTATIONAL METHODS

A. First-principles calculations

For the geometry optimization, ground state, and excited state calculations with constrain DFT (cDFT), we conducted the density functional theory (DFT) calculations with the Heyd-Scuseria-Ernzerhof (HSE) hybrid functional [75], by the Vienna Ab initio Simulation Package (VASP) [76–78]. The defect was constructed and relaxed in $4 \times 4 \times 3$ super cell of ZnO. We use plane-wave cut-off of 400 eV and the projector augmented wave (PAW) pseudopotentials to conduct the structural relaxations. We picked the Fock exchange fraction parameter of 0.375 and screening parameter $\omega = 0.2 \text{ \AA}$, based on reproducing the experimental lattice constants and band gap [79–82]. We obtained band gap 3.4 eV and lattice parameter ($a=3.249 \text{ \AA}$, $c=5.204 \text{ \AA}$) of the pristine zinc oxide, in good agreement with experimental data (band gap 3.4 eV, lattice constants $a=3.25 \text{ \AA}$ and $c=5.21 \text{ \AA}$).

We use the rSCAN functional for the phonon calculation, which is known for its reliability in capturing the static and dynamical properties of the lattice with a low computational cost [38]. We use the Hubbard U correction of 2 eV for the 3d orbital of Zn and obtained the phonon band with very good agreement with experiment

(See SI Fig.7).

B. Defect Formation Energy and Charge Transition Level

In this section we discuss the formation energy of the defects. We follow the standard approach for the computation of formation energy with charged cell correction implemented in JDFTx code [83, 84]. The charged defect formation energy $E_f^q(d)$ of the defect d with charge state q is calculated by

$$E_f^q(d) = E_{tot}^q(d) - E_{tot}(p) - \sum_i \Delta N_i \mu_i + q E_F + E_{corr} \quad (2)$$

where $E_{tot}^q(d)$ is the total energy of the supercell containing the defect with charge state q , and $E_{tot}(p)$ is the total energy of the pristine system in the same supercell as the defect. ΔN_i denotes the difference in the number of atoms of type i between the defect and pristine systems ($\Delta N_i > 0$ means an atom of type i has been added to the defect system and $\Delta N_i < 0$ means that an atom has been removed). μ_i and E_F are the chemical potential of species i and the Fermi energy, respectively. E_{corr} is charged cell correction for eliminating the defect Coulomb interaction with its own periodic images and fictitious homogeneous compensating background [83].

In $\text{X}_{\text{Zn}}\text{V}_{\text{O}}$ defect complex, the third term in Eq. 2 can be written as $\sum_i \Delta N_i \mu_i = -\mu_{\text{Zn}} - \mu_{\text{O}} + \mu_{\text{X}}$. The formation energy of each defect is obtained with chemical potential computed in two conditions: O-rich and O-poor. In the O-rich condition the oxygen chemical potential is computed by total energy of the oxygen molecule ($\mu_{\text{O}}^{\text{O-rich}} = 1/2 E_{tot}(\text{O}_2)$). In the O-poor condition the zinc chemical potential is computed by $\mu_{\text{Zn}}^{\text{O-poor}} = E_{tot}(\text{Zn})$ where $E_{tot}(\text{Zn})$ is the energy of zinc crystal [24]. The $\mu_{\text{O}}^{\text{O-poor}}$ and $\mu_{\text{Zn}}^{\text{O-rich}}$ is computed from $\mu_{\text{Zn}}^{\text{O-poor}}$ and $\mu_{\text{O}}^{\text{O-rich}}$ according to the constrain $\mu_{\text{Zn}}^{\text{O-poor/rich}} + \mu_{\text{O}}^{\text{O-poor/rich}} = \mu_{\text{ZnO}}$. The chemical potential of the dopent X ($\text{X} = \text{Ti}, \text{Nb}, \text{V}$) is computed from its most stable oxide compound, where μ_{Ti} , μ_{Nb} , μ_{V} are computed from TiO_2 , NbO and V_2O_3 respectively [85].

The thermodynamic charge transition level (CTL) between charge states q and q' ($\epsilon(q/q')$) is the Fermi-level position at which the formation energy of charge state q and q' are the same [84, 85]:

$$\epsilon(q/q') = \frac{E_f^q(E_F = 0) - E_f^{q'}(E_F = 0)}{q' - q} \quad (3)$$

where $E_f^q(E_F = 0)$ is the formation energy of defect at fermi-level $E_F = 0$ (aligned with VBM). The defect system is more stable at charge state q when its Fermi-level is smaller than CTL $\epsilon(q/q')$ and is more stable at q' when $E_F > \epsilon(q/q')$.

C. Absorption spectrum and radiative lifetime

The optical absorption spectrum is computed with the Yambo code [86], with the random-phase approximation (RPA) including the local field effect for the polarizability, with the input single particle states from hybrid functional HSE (Fock exchange =0.375) calculations. [87]. The open source plan-wave code Quantum Espresso [88] with norm-conserving Vanderbilt (ONCV) pseudopotentials [89, 90] and wavefunction cutoff of 80Ry has been used for the DFT starting point. We then extract the transition dipole moment and oscillator strength for each excitation. The radiative lifetime for defects transition is derived from the Fermi's golden rule [62, 91] and computed by:

$$\tau_R = \frac{3\pi\epsilon_0 h^4 c^3}{n_D e^2 E^3 \mu^2} \quad (4)$$

where E is the excitation energy, c is the speed of light, μ^2 is the modulus square of transition dipole moment, and $n_D = \sqrt{\epsilon} = 2.4$ is reflective index computed from the dielectric constant of pristine ZnO.

D. BSE and TDDFT

The time-dependent density function theory (TDDFT) [92, 93] and solution of the Bethe-Salpeter equation with quasiparticle energies from GW approximation (GW-BSE) [94, 95] are conducted with starting point at PBE0 functional by the WEST code [96–98]. The projective dielectric eigenpotentials (PDEP) basis set technique [96, 99] was used for the computation of dielectric matrix, screen coulomb potential (W) term in the GW calculation. The convergence of the basis set was reported in SI Figure S9(d) with 60 Ry wave function cutoff. The ZnO band gap computed at GW@PBE0 with $n_{pdep} = 3 \times$ number of electrons is 3.69 eV, close to the zero-point renormalized exciton band gap at zero temperature from experiment (3.6 eV) [100, 101]. The $n_{pdep} = 2 \times$ number of electrons ($2 \times 2496 = 4992$) are chosen as the converged values for the defect calculations.

E. Non-radiative lifetime, Photoluminescent and Huang Rhy's factor

The phonon-assisted non-radiative recombination rate is calculated using Fermi's golden rule as derived in [37]. Under the static coupling and one-dimensional (1D) phonon approximation the recombination rate can be computed by:

$$\Gamma_{NR} = \frac{2\pi}{\hbar} g |W_{if}|^2 \chi_{if}(T) \quad (5)$$

where W_{if} is the electronic coupling term and $\chi_{if}(T)$ is the phonon overlap factor [62]. The phonon overlap $\chi_{if}(T)$ is computed using harmonic oscillator wavefunctions, while the electronic term W_{if} is determined using finite differences of Kohn-Sham orbitals from DFT calculation using HSE(0.375) functional. The non-radiative lifetime, τ_{NR} , is obtained as the inverse of Γ_{NR} . To validate the 1D phonon approximation, we compare the Huang-Rhys factor calculated with the 1D effective phonon and full phonon results, as detailed in the supplementary material SI TABLE S7.

The photoluminescence spectrum was simulated using the all phonon in-house code [47, 102] with $\gamma = 0.005$ eV and smearing = 0.003 eV, where γ is a free parameter that accounts for the broadening of PL. Due to the well-known failure of the GGA and LDA functional on the computation of the ZnO system [25, 103] and the high computational cost of the hybrid function, we applied the rSCAN functional with Hubbard U for the all phonon calculation using Phonopy code interfaced with VASP and Hubbard U correction of $U_{Zn-d} = 2$ eV and $U_{Nb-d} = 3.7$ eV. It has been tested that this method could reproduce the defect local structure comparable to HSE (as shown in SI) as well as the phonon band of pristine ZnO.

F. Decoherence time

Quantum bath model to compute the spin decoherence

We employ the quantum bath theory to compute the spin decoherence [104–106], in which the decoherence occurs due to the entanglement between a central spin and its environment. We consider electronic and nuclear spin baths as the environment. Bath spins are randomly distributed in the lattice and bath spins within a certain radius from the defect qubit are included in the calculation. This bath radius (r_{bath}) is determined by performing a systematic convergence test as shown in Supplementary Figure 1. We find that a radius of 5 nm gives a numerically converged result for the nuclear spin bath. For the electronic spin bath, we find that bath radii of 16, 37, 85, and 220 nm are appropriate for 100, 10, 1, and 0.1 ppm of electronic spin concentrations, respectively.

In addition, we use another parameter (r_{dipole}), which sets the maximum distance for the interaction between bath spins. This means that if two bath spins are separated by a distance larger than r_{dipole} , the two spins are considered as non-interacting. We find that our CCE calculations are converged with r_{dipole} of 1 nm for the nuclear spin bath, and for the electronic spin bath, r_{dipole} of 13, 33, 62, and 120 nm for 100, 10, 1, and 0.1 ppm of electronic spin concentrations.

The dynamics of the total system of qubit and environment is governed by a spin Hamiltonian, which is expressed as:

$$H = H_d + H_{\text{bath}} + H_{d-\text{bath}} \quad (6)$$

where H_d is the qubit Hamiltonian, H_{bath} is the bath spin Hamiltonian, and $H_{d-\text{bath}}$ is the interaction between the qubit and the bath spins. For the nuclear spin bath, each component of the Hamiltonian is given as follows:

$$\begin{aligned} H_d &= -\gamma_e \mathbf{B} \cdot \mathbf{S}, \\ H_{\text{bath}} &= -\mathbf{B} \cdot \sum_i \gamma_{n_i} \mathbf{I}_i + H_{n-n} + H_Q, \\ H_{d-\text{bath}} &= S_z \sum_i \mathbf{A}_i \cdot \mathbf{I}_i \\ &= \sum_i (B_{ix} I_{ix} S_z + B_{iy} I_{iy} S_z + A_i I_{iz} S_z), \\ H_{n-n} &= \frac{\mu_0}{4\pi} \sum_{i,j} \gamma_{n_i} \gamma_{n_j} \left[\frac{\mathbf{I}_i \cdot \mathbf{I}_j}{r_{ij}^3} - \frac{3(\mathbf{I}_i \cdot \mathbf{r}_{ij})(\mathbf{I}_j \cdot \mathbf{r}_{ij})}{r_{ij}^5} \right], \\ H_Q &= \frac{eQ}{6I(2I-1)} \sum_{\alpha,\beta} V_{\alpha\beta} \left[\frac{3}{2} (I_\alpha I_\beta + I_\beta I_\alpha) - \delta_{\alpha\beta} \mathbf{I}^2 \right]. \end{aligned} \quad (7)$$

In these equations, γ_e and γ_{n_i} are the gyromagnetic ratios of the electron spin (\mathbf{S}) and the i -th nuclear spin (\mathbf{I}_i) in the bath, respectively. The external magnetic field is aligned parallel to the defect's symmetry axis. We adopt the secular approximation for the hyperfine interaction ($H_{d-\text{bath}}$), in which the non-secular terms including S_x and S_y are neglected. In the nuclear spin-spin interaction (H_{n-n}), μ_0 is the vacuum permeability and r_{ij} is the distance between the i -th nuclear spin and the j -th nuclear spin.

H_Q is the nuclear quadrupole interaction, in which eQ is the quadrupole moment of the isotope under consideration interacting with the EFG tensor $V_{\alpha\beta}$ ($\alpha, \beta = x, y, z$).

The hyperfine tensor (\mathbf{A}) and the electric field gradient (EFG) tensor ($V_{\alpha\beta}$) are computed by using DFT as implemented in Vienna Ab initio Simulation Package (VASP) code at HSE hybrid functional level of theory. We also use the projector-augmented wave (PAW) [107] pseudopotentials for Zn, O, Nb, and Mo.

The spin Hamiltonian for the electronic spin bath is as follows:

$$\begin{aligned} H_d &= -\gamma_e \mathbf{B} \cdot \mathbf{S}, \\ H_{\text{bath}} &= -\mathbf{B} \sum_i \gamma_{e_i} \mathbf{S}_i + H_{e-e}, \\ H_{e-e} &= -\frac{\mu_0}{4\pi} \sum_{i,j} \gamma_{e_i} \gamma_{e_j} \left[\frac{\mathbf{S}_i \cdot \mathbf{S}_j}{r_{ij}^3} - \frac{3(\mathbf{S}_i \cdot \mathbf{r}_{ij})(\mathbf{S}_j \cdot \mathbf{r}_{ij})}{r_{ij}^5} \right], \end{aligned} \quad (8)$$

Similar to the case of the nuclear spin bath, the qubit Hamiltonian H_d represents the Zeeman interaction of the qubit (electron spin) with an external magnetic field \mathbf{B} .

Here, γ_e is the gyromagnetic ratio of the electron and S_z is the z -component of the electron spin operator. The bath spin Hamiltonian describes the dynamics of the bath spins (other electron spins in the environment). The first term of the bath spin Hamiltonian represents the Zeeman interaction of each electron spin in the bath with the external magnetic field. And H_{e-e} in the bath spin Hamiltonian represents the magnetic dipolar interactions between the electron spins in the bath. Here, \mathbf{S}_i represents the spin operator of the i -th electronic spin in the bath.

The coherence function $\mathcal{L}(t)$ is given as the off-diagonal element of the reduced density matrix, formally expressed as:

$$\mathcal{L}(t) \equiv \frac{\text{tr}[\rho_{\text{tot}}(t)S_+]}{\text{tr}[\rho_{\text{tot}}(0)S_+]} \quad (9)$$

where $\rho_{\text{tot}}(t)$ is the total density matrix of the qubit (ρ_e) and the bath (ρ_{bath}) at time t . S_+ is the electron spin raising operator, defined as $S_+ = S_x + iS_y$. To compute the coherence function, we employ the cluster correlation expansion (CCE) technique [108], which enables a systematic expansion of the coherence function in many-body systems. We find that second-order CCE (CCE-2) and first-order CCE (CCE-1) give numerically converged results for the Hahn-echo decay time (T_2) and the FID time (T_2^*), respectively.

G. ZFS and SOC strength

The zero-field splitting (ZFS) parameters (D and E) consist of first-order spin-spin interaction contributions (D_{SS}, E_{SS}) and second-order spin-orbit (SO) contributions (D_{SOC}, E_{SOC}) [64]. For transition metals, the SO contribution is significant and cannot be neglected. We computed the SO contribution to the ZFS using the linear response method implemented in ORCA [109, 110], employing all-electron PBE0 calculations with the def2-TZVP basis set [111]. In contrast, the spin-spin contribution to the ZFS, which is relatively long-range compared to the SO contribution, did not converge with the cluster size (see SI for the convergence test). To address this, we calculated the spin-spin contribution using our in-house code interfaced with the plane-wave code QUANTUM ESPRESSO [88]. We conducted benchmark calculation for this method using the $(V_{\text{ZnVO}})^+$ system and obtained good agreement with experiments on V^{3+} in ZnO (See SI section XI).

We use the complete active space self-consistent field (CASSCF) method implemented in ORCA [109, 110] to obtain SOC matrix elements between the electronic states. The second order Douglas-Kroll-Hess (DKH2) Hamiltonian [112], the all-electron DKH-def2-TZVP basis set [113], and the SARC-DKH-TZVP basis set [114] are used to account for the scalar relativistic effects. The

spin-orbit mean-field operator is used for the calculation [115]. The cluster is created by retaining atoms near the defects and passivate the surface dangling bond with pseudo hydrogen atoms with core charge of $q=(8-m)/4$ [116], where we choose the O-H bond to be 1.057 Å and Zn-H to be 1.731 Å [117]. More details can be found in SI.

ACKNOWLEDGMENTS

We acknowledge the very helpful discussion with Andrei Faraon, Joe Falson, and Juan Carlos Idrobo. We acknowledge the support by AFOSR CFIRE program under grant FA9550-23-1-0418. This research used resources of the Scientific Data and Computing center, a component of the Computational Science Initiative,

at Brookhaven National Laboratory under Contract No. DE-SC0012704, the lux supercomputer at UC Santa Cruz, funded by NSF MRI grant AST 1828315, the National Energy Research Scientific Computing Center (NERSC) a U.S. Department of Energy Office of Science User Facility operated under Contract No. DE-AC02-05CH11231, the Extreme Science and Engineering Discovery Environment (XSEDE) which is supported by National Science Foundation Grant No. ACI-1548562 [118]. TP and HS were supported by the National Research Foundation (NRF) of Korea grant funded by the Korean government (MSIT) (No. 2023R1A2C1006270), by Creation of the Quantum Information Science R&D Ecosystem (Grant No. 2022M3H3A106307411) through the NRF of Korea funded by the Korea government (MSIT). This material is based upon work supported in part by the KIST institutional program (Project. No. 2E32971).

-
- [1] M. W. Doherty, N. B. Manson, P. Delaney, F. Jelezko, J. Wrachtrup, and L. C. L. Hollenberg, *Physics Reports The Nitrogen-Vacancy Colour Centre in Diamond*, **528**, 1 (2013).
- [2] L. Orphal-Kobin, C. G. Torun, J. M. Bopp, G. Pieplow, and T. Schröder, *Advanced Quantum Technologies* **n/a**, 2300432 (2024).
- [3] I. B. W. Harris and D. Englund, *Phys. Rev. B* **109**, 085414 (2024).
- [4] I. Karapatzakis, J. Resch, M. Schrodin, P. Fuchs, M. Kischnick, J. Heupel, L. Kussi, C. Sürgers, C. Popov, J. Meijer, C. Becher, W. Wernsdorfer, and D. Hunger, *Phys. Rev. X* **14**, 031036 (2024).
- [5] S. A. Tarasenko, A. V. Poshakinskiy, D. Simin, V. A. Soltamov, E. N. Mokhov, P. G. Baranov, V. Dyakonov, and G. V. Astakhov, *physica status solidi (b)* **255**, 1700258 (2018).
- [6] S. Castelletto and A. Boretti, *J. Phys. Photonics* **2**, 022001 (2020).
- [7] A. Gottscholl, M. Kianinia, V. Soltamov, S. Orłinskii, G. Mamin, C. Bradac, C. Kasper, K. Krambrock, A. Sperlich, M. Toth, I. Aharonovich, and V. Dyakonov, *Nat. Mater.* **19**, 540 (2020).
- [8] A. Gottscholl, M. Diez, V. Soltamov, C. Kasper, A. Sperlich, M. Kianinia, C. Bradac, I. Aharonovich, and V. Dyakonov, *Science Advances* **7**, eabf3630 (2021).
- [9] R. Gong, G. He, X. Gao, P. Ju, Z. Liu, B. Ye, E. A. Henriksen, T. Li, and C. Zu, *Nat Commun* **14**, 3299 (2023).
- [10] S. Kanai, F. J. Heremans, H. Seo, G. Wolfowicz, C. P. Anderson, S. E. Sullivan, M. Onizhuk, G. Galli, D. D. Awschalom, and H. Ohno, *Proc. Natl. Acad. Sci. U.S.A.* **119**, e2121808119 (2022).
- [11] Y. Ping and T. J. Smart, *Nat Comput Sci* **1**, 646 (2021).
- [12] D. D. Awschalom, R. Hanson, J. Wrachtrup, and B. B. Zhou, *Nature Photon* **12**, 516 (2018).
- [13] J. R. Weber, W. F. Koehl, J. B. Varley, A. Janotti, B. B. Buckley, C. G. Van De Walle, and D. D. Awschalom, *Proc. Natl. Acad. Sci. U.S.A.* **107**, 8513 (2010).
- [14] J. Falson, D. Maryenko, Y. Kozuka, A. Tsukazaki, and M. Kawasaki, *Appl. Phys. Express* **4**, 091101 (2011).
- [15] Q. Li, J. Zhang, J. Chong, and X. Hou, *Appl. Phys. Express* **6**, 121102 (2013).
- [16] W. Haynes, *CRC Handbook of Chemistry and Physics, 91st Edition* (Taylor & Francis Group, 2010).
- [17] V. Niaouris, M. V. Durnev, X. Linpeng, M. L. K. Viitaniemi, C. Zimmermann, A. Vishnuradhan, Y. Kozuka, M. Kawasaki, and K.-M. C. Fu, *Phys. Rev. B* **105**, 195202 (2022).
- [18] X. Linpeng, M. L. Viitaniemi, A. Vishnuradhan, Y. Kozuka, C. Johnson, M. Kawasaki, and K.-M. C. Fu, **10**, 064061.
- [19] X. Wang, C. Zimmermann, M. Titze, V. Niaouris, E. R. Hansen, S. H. D'Ambrosia, L. Vines, E. S. Bielejec, and K.-M. C. Fu, **19**, 054090.
- [20] M. L. K. Viitaniemi, C. Zimmermann, V. Niaouris, S. H. D'Ambrosia, X. Wang, E. S. Kumar, F. Mohammadbeigi, S. P. Watkins, and K.-M. C. Fu, **22**, 2134.
- [21] X. Linpeng, M. L. Viitaniemi, A. Vishnuradhan, Y. Kozuka, C. Johnson, M. Kawasaki, and K.-M. C. Fu, *Phys. Rev. Applied* **10**, 064061 (2018).
- [22] V. Niaouris, S. H. D'Ambrosia, C. Zimmermann, X. Wang, E. R. Hansen, M. Titze, E. S. Bielejec, and K.-M. C. Fu, *Optica Quantum* **2**, 7 (2024).
- [23] H. Seo, H. Ma, M. Govoni, and G. Galli, *Phys. Rev. Materials* **1**, 075002 (2017).
- [24] A. Janotti and C. G. Van De Walle, *Phys. Rev. B* **76**, 165202 (2007).
- [25] F. Oba, M. Choi, A. Togo, and I. Tanaka, *Science and Technology of Advanced Materials* **12**, 034302 (2011).
- [26] Y. K. Frodason, K. M. Johansen, T. S. Bjørheim, B. G. Svensson, and A. Alkauskas, *Phys. Rev. B* **95**, 094105 (2017).
- [27] S. J. Clark, J. Robertson, S. Lany, and A. Zunger, *Phys. Rev. B* **81**, 115311 (2010).
- [28] Y. Ma, M. Rohlfing, and A. Gali, *Phys. Rev. B* **81**, 041204 (2010).
- [29] V. Ivády, G. Barcza, G. Thiering, S. Li, H. Hamdi, J.-P. Chou, Ö. Legeza, and A. Gali, *npj Comput Mater* **6**, 1 (2020).
- [30] K. Li, V. D. Dergachev, I. D. Dergachev, S. Zhang, S. A. Varganov, and Y. Ping, *Phys. Rev. B* **110**, 184302

- (2024).
- [31] J. R. Reimers, J. Shen, M. Kianinia, C. Bradac, I. Aharonovich, M. J. Ford, and P. Piecuch, *Phys. Rev. B* **102**, 144105 (2020).
- [32] T. J. Smart, F. Wu, M. Govoni, and Y. Ping, *Phys. Rev. Materials* **2**, 124002 (2018).
- [33] B.-C. Shih, Y. Xue, P. Zhang, M. L. Cohen, and S. G. Louie, *Phys. Rev. Lett.* **105**, 146401 (2010).
- [34] J. L. Lyons, J. B. Varley, D. Steiauf, A. Janotti, and C. G. Van de Walle, *Journal of Applied Physics* **122**, 035704 (2017).
- [35] J. J. Markham, *Rev. Mod. Phys.* **31**, 956 (1959).
- [36] J. Walker, *Rep. Prog. Phys.* **42**, 1605 (1979).
- [37] F. Wu, T. J. Smart, J. Xu, and Y. Ping, *Phys. Rev. B* **100**, 081407 (2019).
- [38] J. Ning, J. W. Furness, and J. Sun, *Chem. Mater.* **34**, 2562 (2022).
- [39] A. Alkauskas, Q. Yan, and C. G. Van de Walle, *Phys. Rev. B* **90**, 075202 (2014).
- [40] A. Alkauskas, J. L. Lyons, D. Steiauf, and C. G. Van de Walle, *Phys. Rev. Lett.* **109**, 267401 (2012).
- [41] J. L. Lyons, A. Alkauskas, A. Janotti, and C. G. Van de Walle, *Appl. Phys. Lett.* **111**, 042101 (2017).
- [42] Y. K. Frodason, K. M. Johansen, T. S. Bjørheim, B. G. Svensson, and A. Alkauskas, *Phys. Rev. B* **97**, 104109 (2018).
- [43] A. Alkauskas, B. B. Buckley, D. D. Awschalom, and C. G. V. de Walle, *New J. Phys.* **16**, 073026 (2014).
- [44] O. Bulancea-Lindvall, J. Davidsson, R. Armiento, and I. A. Abrikosov, *Phys. Rev. B* **108**, 224106 (2023).
- [45] M. Mackoiti-Sinkevičienė, M. Maciaszek, C. G. Van de Walle, and A. Alkauskas, *Appl. Phys. Lett.* **115**, 212101 (2019).
- [46] S. A. Tawfik, S. Ali, M. Fronzi, M. Kianinia, T. T. Tran, C. Stampfl, I. Aharonovich, M. Toth, and M. J. Ford, *Nanoscale* **9**, 13575 (2017).
- [47] K. Li, T. J. Smart, and Y. Ping, *Phys. Rev. Materials* **6**, L042201 (2022).
- [48] N. Zhao, S.-W. Ho, and R.-B. Liu, *Phys. Rev. B* **85**, 115303 (2012).
- [49] J. R. Maze, A. Dréau, V. Waselowski, H. Duarte, J.-F. Roch, and V. Jacques, *New J. Phys.* **14**, 103041 (2012).
- [50] R. Nagy, M. Niethammer, M. Widmann, Y.-C. Chen, P. Udvarhelyi, C. Bonato, J. U. Hassan, R. Karhu, I. G. Ivanov, N. T. Son, J. R. Maze, T. Ohshima, Ö. O. Soykal, Á. Gali, S.-Y. Lee, F. Kaiser, and J. Wrachtrup, *Nat Commun* **10**, 1954 (2019).
- [51] B. C. Rose, C. D. Weis, A. M. Tyryshkin, T. Schenkel, and S. A. Lyon, *Diamond and Related Materials* **72**, 32 (2017).
- [52] W. B. Mims, *Phys. Rev. B* **5**, 2409 (1972).
- [53] L.-P. Yang, C. Burk, M. Widmann, S.-Y. Lee, J. Wrachtrup, and N. Zhao, *Phys. Rev. B* **90**, 241203 (2014).
- [54] O. Bulancea-Lindvall, M. T. Eiles, N. T. Son, I. A. Abrikosov, and V. Ivády, *Phys. Rev. Applied* **19**, 064046 (2023).
- [55] L. S. Vlasenko and G. D. Watkins, *Phys. Rev. B* **71**, 125210 (2005).
- [56] X. Zuo, S.-D. Yoon, A. Yang, W.-H. Duan, C. Vittoria, and V. G. Harris, *Journal of Applied Physics* **105**, 07C508 (2009).
- [57] A. S. Fedorov, M. A. Visotin, A. S. Kholobina, A. A. Kuzubov, N. S. Mikhaleva, and H. S. Hsu, *Journal of Magnetism and Magnetic Materials Selected Papers from the Sixth Euro-Asian Symposium “Trends in Magnetism” (EASTMAG-2016)*, **440**, 5 (2017).
- [58] Q. L. Lin, G. P. Li, N. N. Xu, H. Liu, D. J. E, and C. L. Wang, *The Journal of Chemical Physics* **150**, 094704 (2019).
- [59] F. Tuomisto, V. Ranki, K. Saarinen, and D. C. Look, *Phys. Rev. Lett.* **91**, 205502 (2003).
- [60] D. Savchenko, A. Vasin, O. Kuz, I. Verovsky, A. Prokhorov, A. Nazarov, J. Lančok, and E. Kalabukhova, *Sci Rep* **10**, 17347 (2020).
- [61] J. R. Maze, A. Gali, E. Togan, Y. Chu, A. Trifonov, E. Kaxiras, and M. D. Lukin, *MRS Proc.* **1282**, mrsf10 (2011).
- [62] T. J. Smart, K. Li, J. Xu, and Y. Ping, *npj Comput Mater* **7**, 1 (2021).
- [63] M. J. Rayson and P. R. Briddon, *Phys. Rev. B* **77**, 035119 (2008).
- [64] F. Neese, *The Journal of Chemical Physics* **127**, 164112 (2007).
- [65] R. E. Coffman, M. I. Himaya, and K. Nyeu, *Phys. Rev. B* **4**, 3250 (1971).
- [66] G. Filipovich, A. L. Taylor, and R. E. Coffman, *Phys. Rev. B* **1**, 1986 (1970).
- [67] V. Ivády, I. A. Abrikosov, and A. Gali, *npj Comput Mater* **4**, 1 (2018).
- [68] B. N. Figgis and M. A. Hitchman, *Ligand Field theory and its applications* (Wiley-VCH, 2000).
- [69] A. Lenef and S. C. Rand, *Phys. Rev. B* **53**, 13441 (1996).
- [70] M. W. Doherty, N. B. Manson, P. Delaney, and L. C. L. Hollenberg, *New J. Phys.* **13**, 025019 (2011).
- [71] L. Razinkovas, M. W. Doherty, N. B. Manson, C. G. Van de Walle, and A. Alkauskas, *Phys. Rev. B* **104**, 045303 (2021).
- [72] I. B. Bersuker, *J. Phys.: Conf. Ser.* **833**, 012001 (2017).
- [73] G. Thiering and A. Gali, *Phys. Rev. B* **98**, 085207 (2018).
- [74] S. V. Streltsov and D. I. Khomskii, *Phys. Rev. X* **10**, 031043 (2020).
- [75] J. Heyd, G. E. Scuseria, and M. Ernzerhof, *The Journal of Chemical Physics* **118**, 8207 (2003).
- [76] G. Kresse and J. Furthmüller, *Phys. Rev. B* **54**, 11169 (1996).
- [77] G. Kresse and J. Furthmüller, *Computational Materials Science* **6**, 15 (1996).
- [78] G. Kresse and J. Hafner, *Phys. Rev. B* **49**, 14251 (1994).
- [79] M. Thomas, *Chemical Vapor Deposition* **3**, 288 (1997).
- [80] J. Albertsson, S. C. Abrahams, and A. Kvik, *Acta Crystallographica Section B* **45**, 34 (1989).
- [81] F. Oba, A. Togo, I. Tanaka, J. Paier, and G. Kresse, *Phys. Rev. B* **77**, 245202 (2008).
- [82] D. C. Reynolds, D. C. Look, B. Jogai, C. W. Litton, G. Cantwell, and W. C. Harsch, *Phys. Rev. B* **60**, 2340 (1999).
- [83] R. Sundararaman and Y. Ping, *The Journal of Chemical Physics* **146**, 104109 (2017).
- [84] F. Wu, A. Galatas, R. Sundararaman, D. Rocca, and Y. Ping, *Phys. Rev. Materials* **1**, 071001 (2017).
- [85] F. Oba and Y. Kumagai, *Appl. Phys. Express* **11**, 060101 (2018).
- [86] G. Onida, L. Reining, and A. Rubio, *Rev. Mod. Phys.* **74**, 601 (2002).
- [87] D. Sangalli, A. Ferretti, H. Miranda, C. Attaccalite, I. Marri, E. Cannuccia, P. Melo, M. Marsili, F. Paleari,

- A. Marrazzo, G. Prandini, P. Bonfà, M. O. Atambo, F. Affinito, M. Palumbo, A. Molina-Sánchez, C. Hogan, M. Grüning, D. Varsano, and A. Marini, *J. Phys.: Condens. Matter* **31**, 325902 (2019).
- [88] P. Giannozzi, S. Baroni, N. Bonini, M. Calandra, R. Car, C. Cavazzoni, D. Ceresoli, G. L. Chiarotti, M. Cococcioni, I. Dabo, A. Dal Corso, S. de Gironcoli, S. Fabris, G. Fratesi, R. Gebauer, U. Gerstmann, C. Gougoussis, A. Kokalj, M. Lazzeri, L. Martin-Samos, N. Marzari, F. Mauri, R. Mazzarello, S. Paolini, A. Pasquarello, L. Paulatto, C. Sbraccia, S. Scandolo, G. Sclauzero, A. P. Seitsonen, A. Smogunov, P. Umari, and R. M. Wentzcovitch, *J. Phys.: Condens. Matter* **21**, 395502 (2009).
- [89] D. R. Hamann, *Phys. Rev. B* **88**, 085117 (2013).
- [90] M. Schlipf and F. Gygi, *Computer Physics Communications* **196**, 36 (2015).
- [91] F. Wu, D. Rocca, and Y. Ping, *J. Mater. Chem. C* **7**, 12891 (2019).
- [92] Y. Jin, V. W.-z. Yu, M. Govoni, A. C. Xu, and G. Galli, *J. Chem. Theory Comput.* **19**, 8689 (2023).
- [93] Y. Jin, M. Govoni, and G. Galli, *npj Comput Mater* **8**, 1 (2022).
- [94] N. L. Nguyen, H. Ma, M. Govoni, F. Gygi, and G. Galli, *Phys. Rev. Lett.* **122**, 237402 (2019).
- [95] V. W.-z. Yu, Y. Jin, G. Galli, and M. Govoni, *J. Chem. Theory Comput.* **20**, 10899 (2024).
- [96] V. W.-z. Yu and M. Govoni, *J. Chem. Theory Comput.* **18**, 4690 (2022).
- [97] M. Govoni and G. Galli, *J. Chem. Theory Comput.* **11**, 2680 (2015).
- [98] H. Ma, M. Govoni, F. Gygi, and G. Galli, *J. Chem. Theory Comput.* **15**, 154 (2019).
- [99] H. F. Wilson, D. Lu, F. Gygi, and G. Galli, *Phys. Rev. B* **79**, 245106 (2009).
- [100] H. Alawadhi, S. Tsoi, X. Lu, A. K. Ramdas, M. Grimsditch, M. Cardona, and R. Lauck, *Phys. Rev. B* **75**, 205207 (2007).
- [101] S. Tsoi, X. Lu, A. K. Ramdas, H. Alawadhi, M. Grimsditch, M. Cardona, and R. Lauck, *Phys. Rev. B* **74**, 165203 (2006).
- [102] A. Alkauskas, B. B. Buckley, D. D. Awschalom, and C. G. V. de Walle, *New J. Phys.* **16**, 073026 (2014).
- [103] M. D. McCluskey, in *Semiconductors and Semimetals, Defects in Semiconductors*, Vol. 91, edited by L. Romano, V. Privitera, and C. Jagadish (Elsevier, 2015) pp. 279–313.
- [104] H. Seo, A. L. Falk, P. V. Klimov, K. C. Miao, G. Galli, and D. D. Awschalom, *Nat Commun* **7**, 12935 (2016).
- [105] H. Park, J. Lee, S. Han, S. Oh, and H. Seo, *npj Quantum Inf* **8**, 1 (2022).
- [106] J. Lee, H. Park, and H. Seo, *npj 2D Mater Appl* **6**, 1 (2022).
- [107] P. E. Blöchl, *Phys. Rev. B* **50**, 17953 (1994).
- [108] W. Yang and R.-B. Liu, *Phys. Rev. B* **78**, 085315 (2008).
- [109] F. Neese, *WIREs Computational Molecular Science* **2**, 73 (2012).
- [110] F. Neese, F. Wennmohs, U. Becker, and C. Riplinger, *The Journal of Chemical Physics* **152**, 224108 (2020).
- [111] F. Weigend and R. Ahlrichs, *Phys. Chem. Chem. Phys.* **7**, 3297 (2005).
- [112] M. Reiher, *Theor. Chem. Acc.* **116**, 241 (2006).
- [113] D. A. Pantazis, X.-Y. Chen, C. R. Landis, and F. Neese, *J. Chem. Theory Comput.* **4**, 908 (2008).
- [114] J. D. Rolfes, F. Neese, and D. A. Pantazis, *J. Comput. Chem.* **41**, 1842 (2020).
- [115] F. Neese, *J. Chem. Phys.* **122**, 034107 (2005).
- [116] X. Huang, E. Lindgren, and J. R. Chelikowsky, *Phys. Rev. B* **71**, 165328 (2005).
- [117] E. Badaeva, Y. Feng, D. R. Gamelin, and X. Li, *New J. Phys.* **10**, 055013 (2008).
- [118] J. Towns, T. Cockerill, M. Dahan, I. Foster, K. Gauthier, A. Grimshaw, V. Hazlewood, S. Lathrop, D. Lifka, G. D. Peterson, R. Roskies, J. R. Scott, and N. Wilkins-Diehr, *Comput. Sci. Eng.* **16**, 62 (2014).